Final Technical Report

NASA Cooperative Agreement # NCC5-621

Global and Regional Carbon Flux Estimation Using Atmospheric CO_2 Measurements from Spaceborne and Airborne Platforms

1. Overview

We have developed methods for the determination of surface sources and sinks of atmospheric CO2 using inverse modeling from spatially dense atmospheric data anticipated to be available in the near future. These include ubiquitous column CO_2 estimates made from infrared spectra measured by spaceborne sounders (AIRS since 2003, OCO in 2008), and high-precision measurements made from tall towers and aircraft over the continents, as well as more traditional flask sampling. We anticipate that an observing system will emerge with hundreds of thousands of measurements per day around the world permitting regional flux estimation, beginning with very low precision but improving over time. Although they provide a tremendous opportunity for the study of the global carbon cycle, these data challenge us to develop new methods to extract the information.

We have developed and evaluated algorithms for both estimation of CO2 mixing ratio from spaceborne measurements and for quantitative estimation of surface fluxes from concentration data by tracer transport inversion. We have concentrated especially on quantifying potential sources of systematic error or bias in the evolving observing system.

The Colorado State University (CSU) General Circulation Model (GCM) has been used to simulate self-consistent hourly 3D grids of CO2 temperature, water substance and other meteorological variables. The CSU GCM is fully coupled to the Simple Biosphere Model (SiB2), which predicts exchanges of CO2 with the vegetated land surface every six minutes and has been favorably compared to field data at many locations and scales. We compute radiances at the top of the atmosphere in thousands of relevant bands in the infrared and fly virtual satellites through the model

l to sample these radiances. A preliminary study has been completed which has begun to explore the benefits and limitations of retrieving profiles of CO2 employing high resolution measurements from the 1.6 μm region in the near infrared and moderate-resolution measurements in the thermal infrared. This work examined clear-sky scenarios as well as those containing thin cloud. We will further develop and test algorithms for CO2 estimation in the column mean and in several atmospheric slabs from these simulated radiances, including cloud masking, water vapor interference, and a realistic diurnal and seasonal cycle. We have begun using atmospheric inverse methods to estimate regional CO2 fluxes and uncertainty in these fluxes on a monthly basis from the concentration estimated radiometrically. We are also developing possible future strategies for spaceborne CO2 sensors using dedicated hardware, including documentation of requirements for accuracy, sampling frequency, orbital considerations,

etc.

Using the suite of global atmospheric transport responses to regional CO2 pulses available from the TransCom archive, we are evaluating the potential degradation due to transport model error on estimates of regional fluxes obtained by inverse modeling. In this work, we produce pseudo-data using one model, sample the model atmosphere according to OCO and AIRS orbits, bin them into monthly means, and estimate monthly fluxes from each of 22 large regions using transport calculated by 12 other transport models. Preliminary results show substantial bias of flux estimates relative to the (known) "true" flux, and emphasize the need for transport to be simulated with the highest possible fidelity in actual applications.

We are also implementing "nested" regional experiments in the context of the hypothesized ubiquitous satellite CO2 data. These are high-resolution "pseudo-data continent" simulations of North America, South America, and sub-Saharan Africa, simulated with a mesoscale model (SiB-RAMS) on a 40 km grid. We will continue by sampling these fields with "pseudo-aircraft" and "pseudo-tall-towers," and provide guidance about sampling strategies to provide maximum carbon budget constraints with limited resources. These regional optimization studies are seen as collaborative with regional aircraft sampling campaigns proposed in these regions (COBRA and LBA). The Amazon inversions will also include development of improved representations of transport by organized cumulus convection. Preliminary application of these simulations over North America indicate that diurnal biases associated with mid-day sampling of column CO2 are likely to be quite small relative to spectroscopic error expected for the OCO instrument. On the other hand, we find that significant biases are likely to result from clearsky bias, and will have to be modeled.

Mesoscale modeling of atmospheric transport and trace gas concentrations requires specification of lateral boundary conditions from a global model. In collaboration with a group of scientists at NASA GSFC (Randy Kawa, PI), we have developed a system for hourly global CO2 simulations using the Parameterized Chemical Transport Model (PCTM) forced by fossil fuel emissions, air-sea gas exchange estimates, and hourly terrestrial biogeochemistry calculated by SiB. These simulations are still being evaluated against observations, but preliminary results are very encouraging. The intent is to use these global simulations to test methods for global inversions, and to use the resulting concentration field to develop much higher-resolution simulations of continental regions for use in analyzing aircraft data.

2. Description of Activities

2.1. Error Estimation in Atmospheric CO_2 Inversions

A full description of this study was published in the *Journal of Geophysical Research*, **107**, 4635, doi:10.1029/2002JD002195, and is enclosed with this report.

We have investigated the various sources of error in atmospheric CO_2 synthesis inversions using global circulation models, including the estimation of prior, observation, model transport, and representation errors. Failure to account for these errors serves as a *hard constraint* on the inversion and will produce incorrect solutions to the problem, as we show in some simple inversions. The magnitude of these errors falls generally

between about 10% and 100% in the retrieved fluxes, but can be even larger. This makes it highly desirable to avoid hard constraints and apply any prior information we have about the surface fluxes as a weak constraint to the inversion problem. To avoid such pitfalls arising from weak data constraints, most inversion studies have relied on "regularization" techniques. These include truncation of the dimensions of the problem to estimate fluxes from only a few large regions or time averages [e.g., *Fan et al., 1998*]; numerical truncation using singular value decomposition [*Baker, 2001*]; and the use of "prior constraints" in a Bayesian framework [e.g., *Tarantola, 1987*] to penalize solutions which produce unreasonable values [*Rayner et al., 1999*; *Bousquet et al., 2000*; *Gurney et al.*, *2002*]. The inversion formalism commonly used propagates the uncertainty in these prior constraints through the calculation, balancing it against uncertainty in the measurements to obtain the optimized solution. A recent paper by *Kaminski et al., 2001*, (hereinafter referred to as Kam2001) demonstrated that regularizing the solution by spatial truncating (lumping) small basis regions into larger combined ones introduces error. This "aggregation error" was shown to arise because the observed and simulated concentration field may be sensitive to the spatial distribution of sources and sinks within large regions, but the inversion is not free to adjust these subregional patterns. Unlike the Bayesian priors, subregional patterns are typically prescribed in inversions as a "hard constraint." Errors in these patterns cannot be corrected by the inversion procedure, and the resulting error is unavoidably aliased into the resolved sources and sinks. This is not a problem if the pattern of fluxes is correctly known a priori, but in general these patterns cannot be evaluated. To avoid introducing bias in optimized fluxes, Kam2001 recommend using an algorithm that calculates the impact of these errors on the simulated observations used in the inversion. This allows, according to Kam2001, proper accounting for these errors. We showed that is only partly true.

2.1.1. A priori error

Prior constraint on source strengths is needed to avoid unrealistic solutions that arise because of poor data coverage over much of the world given current observing capabilities. These prior constraints include both the global mass-balance of atmospheric CO_2 (known very accurately from the flask record) and estimates of fluxes from each of the regions and months for which fluxes are sought (generally known only poorly). Typical recent inversion calculations have used zero as a prior source estimate for each basis region, with or without a "background" or "presubtracted" field derived from some combination of direct measurement, models, or satellite observations. In the TransCom3 experiment, background fluxes due to fossil fuel emissions [from economic data, *Andres et al., 1996*], seasonal exchange with a balanced terrestrial biosphere [using a model driven by observed climate and satellite vegetation data, *Randerson, 1997*], and air-sea fluxes [interpolated from millions of in-situ measurements, *Takahashi et al., 1999*] were prescribed *a priori*. Prior uncertainty in each of these "presubtracted" fields was assumed to be very small, partly because the fluxes are known rather well relative to other parts of the problem, and partly because corrections to these fields are made in each of the 22 basis regions. Also, neither the neutral biosphere nor the air-sea flux is positive definite, changing signs both over the spatial domain and at given locations through the year. Thus it is not appropriate to simply scale them in the inversion since substantial cancellation would result. Prior estimates of regional fluxes are typically set to zero, with generous

prior error estimates to allow the solution to be data-driven but still prevent spurious dipoles. For annual mean inversions in the TransCom3 experiment, most regions were assumed to have zero fluxes, but some land-use information was also applied [*Gurney et al., 2002*, *2003*]. Prior uncertainty estimates in the oceans were set according to the density of observations used to construct the background flux field [*Takahashi et al., 1999*]. Prior uncertainty on land was set equal to the growing season net flux (sum of all monthly background fluxes during the period when the region is a net sink). Thus the inversion was allowed to double the uptake of a region during the growing season, or to reduce it to zero.

2.1.2. Observation and Mapping Error

The observation error is in general quantifiable by careful calibration of the instruments and laboratory quality assurance programs. Correlations between measurement errors are usually set to zero, allowing the use of a diagonal matrix for the covariance matrix. Analytic error in CO_2 mole fraction is assessed by calibration and analysis of samples of known quantity in blind tests. This source of error is small, generally within 0.05 ppmv [*Masarie et al., 2001*]. Other important sources of direct observation error are introduced by sample collection processing equipment, and by the fact that interlaboratory calibrations across the network are difficult to maintain. The latter source of error is likely the most significant, and is regularly assessed by round robin comparisons of analyses of common flask samples by multiple laboratories. Interlaboratory differences are believed to contribute at least 0.2 ppmv uncertainty in measured mole fraction. [*World Meteorological Organization, 1995, 1999*].

When we include any remote observations of CO_2 in the inversion, we need to include a mapping error covariance. This describes the error caused by retrieving a CO_2 concentration from an indirect observation (e.g., satellite observed radiances). In its simplest form it is just the retrieved CO_2 uncertainty, comparable to the observation error covariance. However, if the indirect observations are used directly in the inversion, this covariance matrix describes the errors in the mapping operator (e.g., a forward radiative transfer model). The first form would come directly from a CO_2 retrieval algorithm, the second form would have to be estimated by comparing the used mapping operator to similar or better mapping operators (e.g., a fast radiative transfer model could be compared to a line-by-line radiative transfer model). A possibly serious error arises when the observation errors are correlated in space and/or time. For instance, satellite observations could be dependent on the surface albedo. If we do not know this surface albedo accurately, the retrieved CO_2 concentrations over land could be biased with respect to the retrieved CO_2 concentrations over ocean. These regional biases can introduce error in the retrieved fluxes, since they create non-existent spatial gradients. It is therefore crucial to be aware of any biases in the observations.

2.1.3. Transport Error

The transport error is a very important contributor to the overall error budget of CO_2 inversions, whose importance is likely to be amplified as additional observations become available [*Denning et al., 2001*]. It can be split up into two components: the transport model error and the transport model parameter error. The first error represents any simplification of the real physics and dynamics in the transport model (e.g., convective

parameterizations). This first transport model error tends to be systematic and is generally hard to estimate, since we can not exactly model the real world dynamics and physics. However, comparisons with high-resolution transport models (e.g., numerical weather forecast models) can give an estimate of this bias. The second error (transport model parameter error) represents the effect of errors on any model parameter. We have used the variance in the Jacobian of the transport operators across the suite of 16 models used in the TransCom experiment as a first estimate of the effect of transport error on errors in the recovered fluxes by region. We showed that specification of transport error in the covariance matrix of the optimization algorithm can reduce the bias in flux estimates, though it necessarily increases the a posteriori uncertainty in the result.

2.1.4. Representation Error

We define two types of representation error involved in CO_2 inversions, the internal and external representation error. The internal representation error describes the errors that arise when we perform the CO_2 model inversion on a different grid (both space and time) than the transport model grid. This inversion grid can be just an aggregation of grid boxes, but is more commonly a representation of the surface fluxes on large basis regions [e.g., *Gurney et al., 2002*, *2003*]. The error represents the mismatch in resolution between the forward model calculations to obtain the transport operator (e.g., 72 by 44 grid boxes on 30-minute time intervals) and the inversion performed on the monthly means of for instance 22 basis regions. It was this source of error that was investigated by Kam2001, and termed aggregation error. The external representation error involves mismatches between the model simulation and the observations, in both space and time.

Flask samples are taken from a continuously varying concentration field, and are influenced by many factors not present in the transport models used for typical inversions. External representation error includes spatial variations at scales smaller than the model grid boxes, and time variations at scales shorter than the sampling frequency of the observations. Many inversions optimize simulated monthly mean concentrations over areas as large as 10^5 km^2 through depths of up to 1 km against point samples taken at the surface once a week, for example. External representation error may also include unresolvable transport due to synoptic, mesoscale or local phenomena. Local- or regional-scale emissions or sinks (for example, a factory or power plant in a particular direction from a sampling site) that cannot be correctly represented in a model also lead to errors of this kind. Sampling protocols are designed to obtain background air that is representative of large upstream regions and as free as possible from local influences or contamination. Conditional sampling of model simulations to mimic these protocols may be appropriate in some cases to reduce external representation error. Many flask observation stations are located along coastlines, and the sampling protocol specifies a "clean air sector" from which the wind must be blowing for valid samples of background air to be taken. An example is Point Barrow, located on the Arctic coast of Alaska. Global models cannot resolve the mesoscale weather and concentration gradients in such a location, which by definition must lie at the edge of a grid cell. Spatial interpolation between the marine grid cell to the north and the land grid cell to the south would necessarily introduce just the kind of local terrestrial influence that the sampling protocol attempts to prevent. An alternative is to track these influences in the model, by simulating a tracer emitted only on land, such as ^{222}Rn [*Ramonet et al., 1996*]. Monthly means can

then be computed and used in response functions during only those clean air periods when the ^{222}Rn concentration was below some threshold. Several studies have assessed the impact of sampling the model output to better reflect the conditions of sample collection [*Ramonet et al., 1996, Law, 1996*]. The impacts on estimated fluxes by inversion can be substantial when compared with results using simulated concentrations inland grid cells to represent baseline conditions, but are small compared to simply sampling an adjacent grid cell offshore (e.g., *Gurney et al., 2002*, *2003*).

In atmospheric CO_2 inversions it is important to account for all relevant sources of error. These errors are split into two categories, the a priori errors defining our confidence in the a priori estimate of the surface fluxes, and the errors representing the expected difference between the model simulations and the observations. The latter category of errors should contain several different sources of error, although quite often only the observation error is taken into account. This leads in the best case to misleading discussions about the value of the observations and in the worst case to incorrect inversion results. Not accounting for certain error sources can be defined as applying hard constraints to the inversion problem. A hard constraint uses prior information relevant to the inversion problem and applies it without any flexibility in case the prior assumptions are wrong. In most cases this will lead to incorrect inversion results. On the other hand, a weak constraint also applies prior information to the inversion problem, but allows flexibility to these assumptions within the margins of the defined a priori error covariance. If estimated correctly, these prior assumptions and especially these prior covariance matrices will constrain the problem correctly. It is important to note here that using prior information with very small prior error estimates in cases where this is not justified basically acts as a hard constraint as well. We examined two sources of error that are often applied as hard constraints, the model transport error and the internal representation error. When the model transport error is not taken into account, we assume a perfect relation between CO_2 concentration observations and surface fluxes. This will give too much weight to the observations in the inversion. Proper accounting for the model transport error will give proper weights to the observations depending on how well our transport model is able to model regional and large-scale transport. So, even perfect observations will have to be weighted properly depending on how well our transport model is able to model the relationship between these observations and the surface fluxes.

The internal representation error is harder to deal with, because it cannot be completely accounted for. Specifying fixed footprints in large regions or seasonal or diurnal patterns of fluxes will limit the possible solutions to the inversion problem to exactly those assumed patterns. Only the amplitudes of these footprints can be changed during the inversion. If the assumed flux pattern is can lead to incorrect aggregrated fluxes for each basis incorrect, the solution within each basis region will be incorrect, which region. Also the specification of an a priori constraint with very small a priori errors, as was done in the TransCom3 experiment with the neutral biosphere and the fossil fuel fluxes, will often lead to incorrect results if these small a priori errors are not justified. Most optimal would be to invert on the native transport model grid and time step with the prior knowledge of the fluxes fully specified as a weak constraint. This allows for an optimal use of the information contained in the observations. If the observations contain little information about the fluxes in a certain area, the retrieved fluxes will basically reflect the prior estimate. If the observations do contain information

about the fluxes in a certain region, the fluxes in that region will be adjusted to match the simulated concentrations with the observations. Proper inversion statistics (e.g., averaging kernels [*Rodgers, 2000*]) will show where we retrieve the prior estimates back and where we will retrieve new information about the fluxes. This also allows for a more continuous improvement of our flux estimates when more and better observations become available. However, with the current transport models this is hard to accomplish, especially since most of these models do not have an adjoint model. The calculation of the response functions for every grid box and time step would therefore be a very cumbersome task. We recommend, however, to be aware of the possible representation errors and to make an effort to minimize these errors by using a spatial and temporal grid for the inversion that is closer to the native model grid than is currently used. Downscaling the inversion problem by using large regions and assumed temporal patterns is too rigid and leads to unavoidable bias in the retrieved fluxes. Especially, with increased flask measurement programs and the next generation satellites providing many more observations [*Engelen et al., 2001*, *Rayner et al, 2002*] modelers should make an effort to make full use of these observations and avoid any hard constraints on the problem. Finally, we would like to point out the use of full data assimilation systems. These would allow a better use of the current and future observations by using observations when and where they are available to constrain the forward model run. This way we could even constrain biological surface flux processes (if modeled in the data assimilation model) with such observation as satellite surface vegetation maps or ocean surface chlorophyll concentrations. Although this kind of full data assimilation to invert surface CO_2 fluxes may still be years down the road, we think it is important to head in that direction and start thinking how to make best use of the available observations.

2.2. Retrieval Development and Error Estimation

This section presents research on CO_2 retrieval and error estimation conducted collaboratively with both the OCO Science Team and with NOAA-sponsorship. Portions of this work have been published by Engelen et al (2001) and Christi and Stephens (2004), both of which are attached. [Note that the latter manuscript erroneously failed to acknowledge funding from NASA. An addendum is being sought with AGU to correct this oversight.]

We are exploring the feasibility of retrieving atmospheric CO_2 concentrations from atmospheric infrared soundings available from space-borne instruments. Both the Atmospheric Infrared Sounder (AIRS) and the Infrared Atmospheric Sounding Interferometer (IASI) measure most of the infrared spectrum at high spectral resolution. IASI [*Diebel et al., 1996*] is a Michelson interferometer with a spectral resolution of 0.5 cm^{-1} in the spectral range between 645 and 2760 cm^{-1} and is expected to be launched on board of the first Meteorological Operational polar satellite (METOP) in 2003. AIRS [*Aumann and Miller, 1995*] is an echelle spectrometer that covers the spectral range between 650 and 2700 cm^{-1} with an average resolving power of 1200 and is deployed on board of EOS-Aqua. The satellites of both instruments will fly in sun-synchronous orbits providing 2 observations per day for each location on Earth (taking into account the cross-track scanning of the instruments).

The above 2 instruments have been designed to measure accurate temperature and water vapor profiles on a global scale, but their high spectral resolution observations offer

great opportunities to measure other atmospheric gases as well. Two strong CO_2 absorption bands exist at 667 and 2350 cm^{-1}, respectively. The water vapor and CO_2 absorption spectra are shown in Figure 12a. In the past, these bands have been used to retrieve temperature profiles assuming a well-known atmospheric CO_2 concentration. However, with the above-mentioned high spectral resolution observations temperature, water vapor, and CO_2 can be retrieved simultaneously.

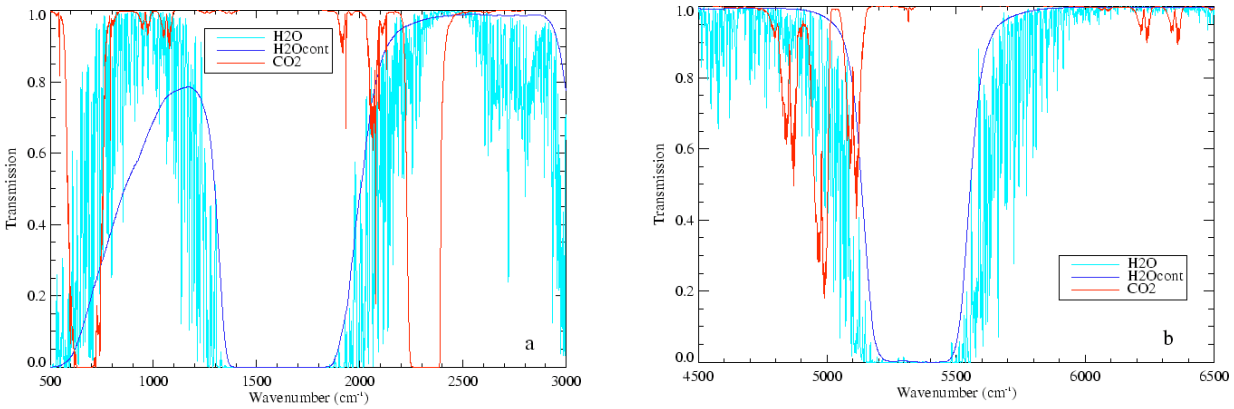

Figure 1. Absorption spectra of water vapor and carbon dioxide in the infrared (a) and near infrared (b) part of the spectrum.

Another technique to measure CO_2 that is being analyzed uses sunlight reflected in the near infrared (NIR). Aoki et al. [1993] describe a retrieval scheme that uses the reflected solar radiation in sun glint situations over oceans to retrieve several trace gases with high accuracy. In those situations the atmospheric contribution to the radiation observed at the top of the atmosphere is much smaller than the surface contribution and can therefore be neglected. This simplifies the radiative transfer considerably, which allows for accurate total column measurements of CO_2 and H_2O in the spectral region between 1.5 and 2.2 μm (4500 and 6500 cm^{-1}). Their absorption spectra in this spectral region are shown in Figure 12b. We will investigate the capabilities of this method not only in sun glint situations over ocean, but also over land. A key issue is the relative contribution of the atmospheric term in the radiative transfer with respect to the surface contribution.

2.2.1. Forward Radiative Transfer Models

Two models were employed to simulate the measurements in the retrieval: one for the near infrared (NIR) and one for the thermal infrared (IR). The plane-parallel, multiple-scattering model used to compute the monochromaticradiances in the 1.6μm region of the NIR follows the transfer matrix method (see e.g. *Benedetti, 2002*). In simulating radiances from this region, only gaseous absorption from CO_2 was considered since the strongest absorption lines other than CO_2 at the wavenumbers chosen from this region are affiliated with water vapor whose line strengths are two orders of magnitude below that of CO_2. Although there is some claim that water vapor may still need to be included in this region [*Buchwitz, et al., 2000*], it was not considered in this preliminary study. The forward model used to simulate the IR measurements is the same used by *Engelen et al., 2001*. The algorithm incorporates a Malkmus band model to obtain the optical depth and resulting transmission produced by different atmospheric gases. In this region, influences

of CO_2, H_2O, and O_2 are considered and radiances are computed at a 1 cm^{-1} spectral resolution. Unlike the NIR model however, the model performs computations for non-refracted paths only. In both the IR and NIR, nadir viewing was employed.

2.2.2. Retrieval Method and Setup

Simulations of retrieving a CO_2 profile utilized the method of optimal nonlinear inversion as set forth by *Rodgers, 2000*. The measurements are weighted along with a constraint a priori CO_2 profile where the estimated errors in both the measurements and a priori are used as weights.

Synthetic measurements used in the retrieval were taken from 6203.400-6221.475 cm^{-1} from the 1.6 μm CO_2 absorption band of the NIR at a resolution of 0.025 cm^{-1} (724 channels) and from 500-2500 cm^{-1} in the IR at a resolution of 1 cm^{-1} (2000 channels). The underlying surface is assumed Lambertian with a surface temperature of 296K and with different surface albedos chosen to observe their affect. In this study, the measurement error covariance was assumed diagonal (i.e. measurement error at one wavenumber is assumed independent of measurement error at other wavenumbers). In the NIR, the instrument is given to have a CO_2 continuum signal-to-noise ratio (SNR) of 400:1 at a surface albedo $\alpha = 0.06$ and solar zenith angle $\theta = 22^{\circ}$. This SNR is similar to that used in Kuang [2002]. Since high resolution measurements appear required for the measurement of CO_2 [O'Brien and Rayner, 2002], the instrument in the NIR is given to have a δ-function response in this preliminary study. This will provide an upper bound on what the NIR measurements can be expected to provide. In the IR, the instrument is given to have a SNR of 200:1 at each wavenumber. This is the same as used in *Engelen et al., 2001*. Furthermore, the atmospheric profiles of temperature, water vapor, and ozone are assumed to be known perfectly; thus, there is no contribution to error in transmission due to these constituents on the measurements in the IR. The a priori covariance is assumed symmetric with the error associated with the a priori at a given level assumed correlated with errors at other levels in an exponentially decreasing fashion. The actual variances used on the diagonal of the a priori covariance for levels above 500 hPa are based on the work of *Schmidt and Khedim, 1991*. The variances used for CO_2 concentrations below 500 hPa were designed to reflect the larger CO_2 variations in this region. In particular, the variance estimated for the surface is based on CO_2 measurements taken from tall towers (e.g. see *Bakwin et al, 1995, 1999*). Of course, upon implementing such ideas in an operational framework, the error statistics of the a priori profile could be more finely determined using the results of prior retrievals over each locale, thus yielding a more precise a priori for that locale.

2.2.3. Retrieval Results

The CO_2 profile used in the retrieval simulations is meant to typify the kind of profile one would expect to find downwind of a source of atmospheric CO_2. It was generated by the Colorado State University GCM and corresponds to the eastern coast of the United States and is the same as used in *Engelen et al., 2001*. The atmospheric profiles of temperature and pressure as well as density of air, water vapor, and ozone in which the CO_2 profile is embedded are from [*McClatchey et al., 1972*] and correspond to midlatitudes summer conditions. For these retrievals, the surface albedo and solar zenith angle are assumed known. Also, the surface albedo is assumed to remain constant across the 18.075 cm^{-1} spectral band used from the NIR. This allows us to focus on what role the IR and NIR measurements are contributing to the retrieval as well as the potential problems caused by thin cloud.

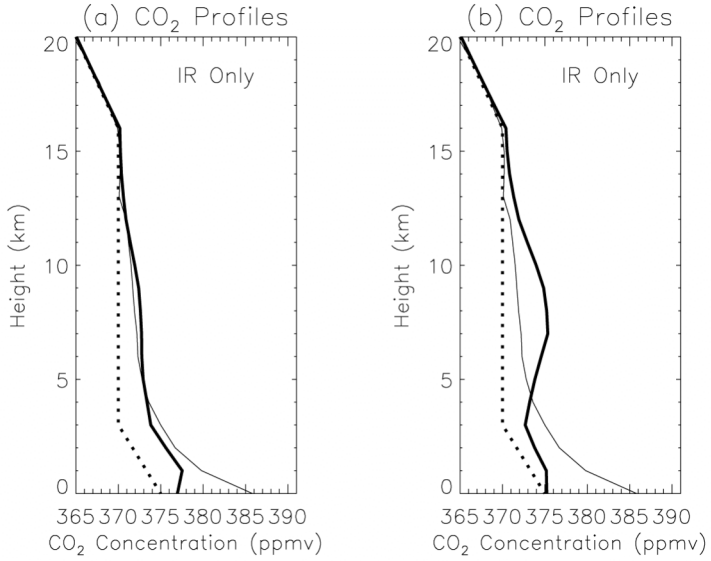

Figure 2: Retrievals of a source profile of CO_2 using only IR measurements. The retrieval was performed in (a) clear sky and (b) the presence of a cirrus cloud at 13 km with $\tau_c = 0.10$ in the NIR and $\tau_c = 0.05$ in the IR. Shown are the real (thin solid), retrieved (thick solid), and a priori (dotted) CO_2 profiles.

Retrievals of a CO_2 Profile in Clear Sky

Figure 13(a) reveals the results of retrieving CO_2 in clear-sky using only IR measurements. The real CO_2 profile is the thin solid line, the retrieved profile the thick solid line, and the a priori profile dotted. One observes from the figure that the retrieved profile holds the real profile fairly well down to about 3 km, but diverges from there down to the surface where the IR measurements are insensitive to CO_2. Figure 14 also shows the results of retrieving CO_2 in clear-sky, but this time using only NIR measurements (upper row) and IR and NIR measurements together (lower row). The profiles in each plot are denoted the same as in Figure 13. Since the measurements in the NIR are due to reflection of the sun's radiation from the underlying surface, the solar zenith angle and surface albedo are also specified. In these simulations, the solar zenith angle is set to 30˚ while the surface albedo takes on values of 0.003, 0.03, and 0.3 as one moves across each row in the figure from left to right.

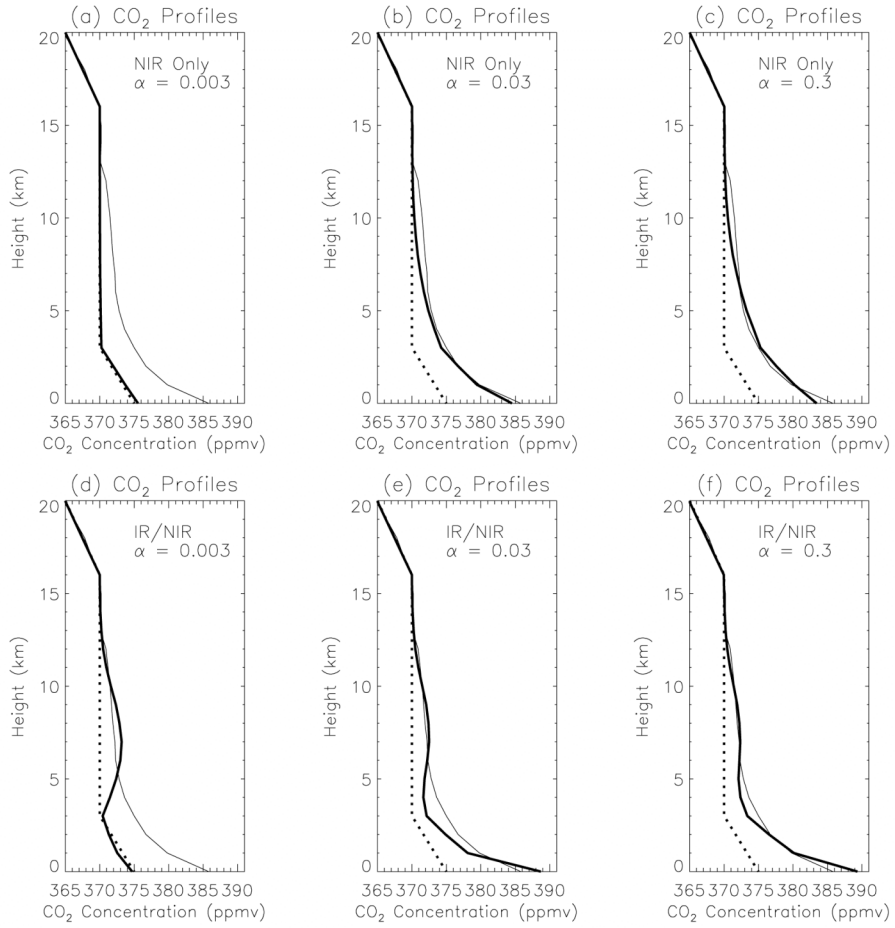

Figure 3: Retrievals of a source profile of CO_2 in clear sky obtained by using only NIR measurements (upper row) and both IR and NIR measurements (lower row). The curves are the same as in Figure 13.

As a part of this study, sensitivities of radiances from the 1.6μm spectral band to CO_2 as well as to scatterers such as thin cloud and aerosol were explored under various combinations of solar zenith angle and surface albedo. In particular, it was found that the sensitivity of the radiances to CO_2 as surface albedo varied fell within three regions: for $0 < \alpha < 0.01$ ("region 1"), the sensitivity showed significant decrease as α approached 0; for $0.01 < \alpha < 0.05$ ("region 2"), the sensitivity showed marked decrease as α approached 0.01; and for $\alpha > 0.05$ ("region 3"), the sensitivity remained fairly constant. In a forthcoming paper, we will show these results among others in greater detail. Here, the values of albedo were chosen as a sample from each of these regions of CO_2 sensitivity. Looking at the upper row of Figure 14 where only the NIR is used, one observes that when the albedo is 0.003, the measurements are overcome by noise and Rayleigh scatter and the retrieval merely returns the a priori profile; however, in the latter two cases when the albedo is 0.03 and 0.3, respectively, the enhanced returns from the surface yield much better results with small errors exhibited throughout the troposphere. Turning attention next to (d) where both the IR and NIR are now in use, we notice improvement over the NIR only case in (a) owing to the contribution now provided by the IR in the mid and upper troposphere, but that it is not as good as the IR only case in Figure 13(a) due to the fact that some weight is placed on the NIR measurements which in this case are poor. In contrast the results in (e) and (f), where the albedo is 0.03 and 0.3, are rather good except for the bulge in the 1-5 km region in (e) and the 2-6 km region in (f). The bulge is the result of the retrieval striking a compromise between the contributions made by both the IR and NIR measurements. As evidence of this, compare

the retrieved profile in (e) with (b) above it and with (a) in Figure 13. In the region 5 km and up, the IR and NIR are working in harmony, whereas in the 0-5 km region, there appears a struggle for control of the retrieval with the IR measurements appearing stronger to some degree in this instance. One the other hand, the result in (f) seems to indicate the opposite where the NIR measurements appear to exert greater influence due to increased surface returns.

Retrievals of a CO_2 Profile in the Presence of a Thin Cirrus Cloud

The results of retrieving the CO_2 source profile in the presence of an undetected thin cirrus layer are given in Figure 13(b) and all plots in Figure 15. For this part of the study, a cirrus cloud was placed at 13 km in the atmosphere with an optical depth of $\tau_c = 0.10$ in the 1.6 μm region of the NIR. Since the amount of scattering in the IR is small, the cloud was approximated in the IR as a totally absorbing layer. The optical depth of the cloud in the IR was assigned based on the ratio of absorption to extinction efficiency as one moves into the IR portion of the spectrum (≈ ½). Using this approximation, τ_c is assigned a fixed value of 0.05 across the IR. Regarding scattering properties, the cloud was chosen to have an asymmetry factor of 0.77 and a single scatter albedo of 0.97 in the NIR. This corresponds to a cirrus cloud with ice crystals with a mean effective size of 10μm [Lynch et al, 2002]. The Henyey-Greenstein phase function was prescribed to characterize the cloud and aerosol's pattern of scatter. Although the Henyey-Greenstein is not totally adequate to describe the scattering pattern of an ice cloud, which are notorious for having complex phase functions, the Henyey-Greenstein was chosen as in O'Brien and Rayner, 2002 to provide a reasonable upper bound on the scattered radiance. Figure 13(b) reveals the CO_2 profile retrieved in the presence of the undetected thin cloud using only the IR. We observe that the affect of the cloud is to raise the effective level of emission. The retrieval produces an increased CO_2 concentration in the upper troposphere as a result. Since the

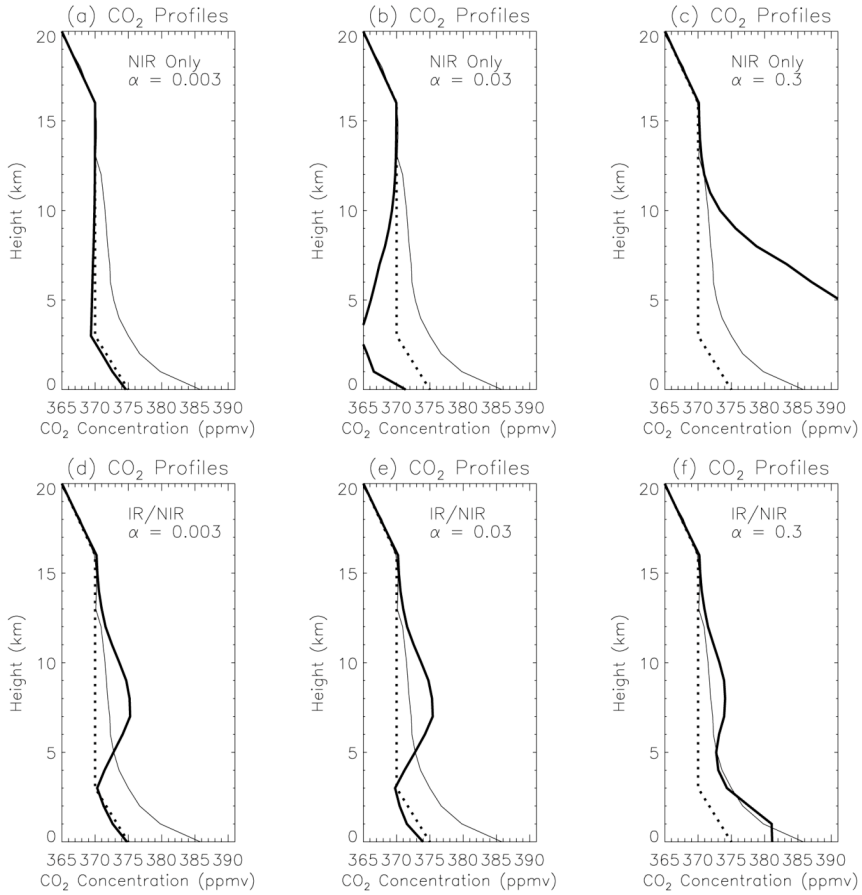

Figure 4: The same as Figure 14 except retrievals performed in the presence of an undetected cirrus cloud at 13 km with $\tau_c = 0.10$ in the NIR and $\tau_c = 0.05$ in the IR.

excess CO_2 in the 4-12 km region in part compensates for the deficiency in the 0-4 km region, the overall result is a CO_2 column-average value that is actually an improvement over the result in (a) of the same figure, despite the degradation in the retrieved profile (compare "IR only" results in Table 1). Figure 15 again shows the results of simulating the retrieval of CO_2 using the NIR only (upper row) and IR and NIR together (lower row), but now in the presence of the undetected thin cloud. The values of solar zenith angle and surface albedo are the same as in Figure 14. Looking at the upper row of this figure, one observes that when the albedo is 0.003, the retrieval (as expected) again returns the a priori profile; however, unlike Figure 14, (b) and (c) show that when the albedo is 0.03 and 0.3, the retrieval is seriously damaged by scatter induced by the thin cloud. The results in (b) and (c) can be understood in the following way. During the NIR sensitivity study, the sensitivity of the radiances to scatterers such as thin cloud and aerosol was also investigated. It was discovered that the NIR radiances could be suppressed by up to 5% or enhanced by up to 50% depending on the solar zenith angle, surface albedo, and the optical depth and altitude of the scatterer. In some instances, the scattering layer functioned more as a barrier to solar photons entering the region below the scatterer, whereas in other instances, it tended to function more as a trap, thereby impeding the return of photons from the region below the scatterer and allowing them to be subjected to more absorption in the more CO_2 rich region below the scatterer. Plots (b) and (c) give testimony to this type of behavior. In (b), the thin cloud is functioning more as a barrier, thus giving the retrieval the illusion of a CO_2 deficiency in the troposphere. In (c), the thin cloud functions more as a trap, thus allowing more photon absorption and the illusion of an unrealistic CO_2 abundance.

Turning attention to (d) where both the IR and NIR are again in use, we note some improvement over the "NIR only" case above it owing to the contribution provided now by the IR measurements in the mid and upper troposphere, but that it is still inferior to the IR only case in plot (b) of Figure 13 due to the fact that some weight is placed on the NIR measurements which are still poor. Likewise, the retrieved profile in (e) is not much better - particularly due to the interference of the thin cloud on the NIR measurements combined with modest surface returns. In contrast, the result in (f) is much better due to both improved surface returns in the NIR along with some constraint provided by the IR measurements. Except for some deviation in the 6-11 km region and next to the surface, the retrieved profile characterizes the nature of the true CO_2 profile fairly well.

CO_2 Column-average Values

The column-average value of CO_2 volume mixing ratio (q) for the real, a priori, and retrieved CO_2 profiles are shown in Table 1 along with the associated error (Δq) in the a priori and retrieved profiles. The retrieved profiles are indicated by the measurements used in the retrieval, the scene in which it was retrieved (clear sky or in the presence of thin cloud), and the stipulated surface albedo.

Profile	Scene	α	q	Δq
Real	-	-	373.43	-
a priori	-	-	370.20	-3.23
IR only	CLEAR	-	372.69	-0.74
NIR only	CLEAR	0.003	370.36	-3.08
NIR only	CLEAR	0.03	372.93	-0.51
NIR only	CLEAR	0.3	373.39	-0.05
IR/NIR	CLEAR	0.003	371.12	-2.31
IR/NIR	CLEAR	0.03	372.84	-0.59
IR/NIR	CLEAR	0.3	373.39	-0.05
IR only	CLOUD	-	372.84	-0.59
NIR only	CLOUD	0.003	369.85	-3.59
NIR only	CLOUD	0.03	367.07	-6.37
NIR only	CLOUD	0.3	388.37	+14.93
IR/NIR	CLOUD	0.003	371.78	-1.65
IR/NIR	CLOUD	0.03	371.51	-1.92
IR/NIR	CLOUD	0.3	373.83	+0.40

Table 1: Column-average values of CO_2 volume mixing ratio (in ppmv) for real, a priori, and retrieved profiles along with associated error. Retrieved profiles are indicated by the measurements used, the scene (clear or with cirrus clouds), and albedo given in which the profile was retrieved.

We observe that the "IR only" CO_2 retrieval performs well in clear sky or the presence of thin cloud with the value of q improved slightly in the case of thin cloud for the reasons cited earlier. Also, the "NIR only" retrieval outperforms the "IR only" or "IR/NIR" retrievals in clear sky when the surface albedo was 0.03 or 0.3; otherwise, the value of q was either only marginally better or was even worse than the a priori. In contrast, all the values of q obtained via the "IR/NIR" CO_2 retrieval fall within the estimated 2.5 ppmv margin of error required with the "IR/NIR" retrievals outperforming the "IR only" retrievals in the presence of a brighter surface ($\alpha = 0.03$ or 0.3 in the clear sky case or $\alpha = 0.3$ in the cloudy case) due to increased CO_2 sensitivity near the surface in the NIR.

This study was performed to investigate the possible benefits and limitations of retrieving profiles of CO_2 by employing high-resolution measurements from the 1.6 μm region in the NIR and moderate-resolution measurements in IR. Two sets of experiments were performed to begin to assess these benefits and limitations. The results of this study show that they can work in a complementary fashion in retrieving these profiles. In the clear-sky cases, retrievals using only the NIR outperformed those using only the IR or

using both the IR and NIR together in retrieving the CO_2 profile when the albedo fell into regions 2 or 3; however, the retrieval using only the IR performed better when the albedo fell into region 1. In the presence of an undetected thin cloud however, the scattering experienced by NIR photons rendered large errors in the retrieved CO_2 profile. In contrast, the retrieval using both the IR and NIR together gave a satisfactory profile when the albedo fell into region 3 where the IR appears to serve as an agent of stability. Although additional work is required to examine the behavior of retrieved CO_2 profiles and their resulting column-average values in greater detail with more robust parameters and assumptions, given that the optical depth of the simulated cloud was small ($\tau_c = 0.10$ in the NIR and 0.05 in the IR), it appears (1) a fairly accurate means of determining atmospheric scatterers and (2) higher surface albedos will generally be required to realistically obtain the best quality information of CO_2 concentration on a global scale. In addition, due to greater sensitivity of the NIR to CO_2 in the lower atmosphere and the stability provided by the IR, it would appear wise to consider utilizing them both together in any future CO_2 satellite mission so that the best results may be obtained as the measurements are subjected to the variety of conditions experienced in the real atmosphere.

2.2.4. Spatial Distribution of OCO Measurements

Because OCO requires that the sky be 'almost clear' in order to measure , data from the Geoscience Laser Altimeter System (GLAS) was used to identify targets in the following categories:

1. totally clear sky (no aerosol or cloud detected by the algorithm);
2. no cloud but aerosol optical depth between zero (excluded) and a threshold;
3. no aerosol but cloud optical depth between zero (excluded) and a threshold;
4. total optical thickness of aerosol and cloud between zero (excluded) and a threshold.

The optical thickness threshold beyond which accurate measurements of CO_2 become impractical is not known precisely, but is likely to be about 0.2, so this value was chosen as the threshold.

The frequency of totally clear sky, which globally averaged is approximately 15%, has very strong spatial variations, both zonal and longitudinal. A large fraction of the clear cases occur over the deserts of both hemispheres in the downward branches of the Hadley cells. The clearest areas, however, are found over the ice caps of Greenland and Antarctica, partly because these areas have very low amounts of aerosol. Regions with the lowest clear fractions are the storm tracks of mid-latitudes in both hemispheres, and regions of oceanic stratocumulus (east of the oceanic subtropical basins).

Cases with no cloud but some aerosol are fairly common; of the cases without cloud, over half have an aerosol layer, except at high latitudes. Furthermore, over the oceans the bulk of the aerosol is in the boundary layer, with mean height less than 1 km. This is good news for OCO, because boundary layer aerosol has a lesser effect upon photon path length distributions, and therefore is less likely to bias estimates of . In contrast, aerosol layers are observed several kilometres above land surfaces.

Cases with thin cloud but without aerosol are less common. Maximum frequencies are on the order of 10% in some areas of the tropics as well as high latitudes, but at mid-latitudes the frequency is low. These results indicate that the semi-transparent high-clouds that are frequently observed by passive sensors generally have an optical thickness larger than the threshold. As expected, these thin cloud layers are much higher than the aerosol layers, exceeding 10 km in the tropics. Consequently, these cases are likely to be more difficult to analyze, because high cloud generally shortens the photon path length.

Finally, the frequency of almost clear cases, shown in Fig 5, exceeds 30% for a large fraction of the tropics, and in the band from 40N to 40S the almost clear atmospheres are about twice as numerous as the totally clear cases. Furthermore, the spatial distribution of the almost clear cases is tightly correlated with the totally clear cases.

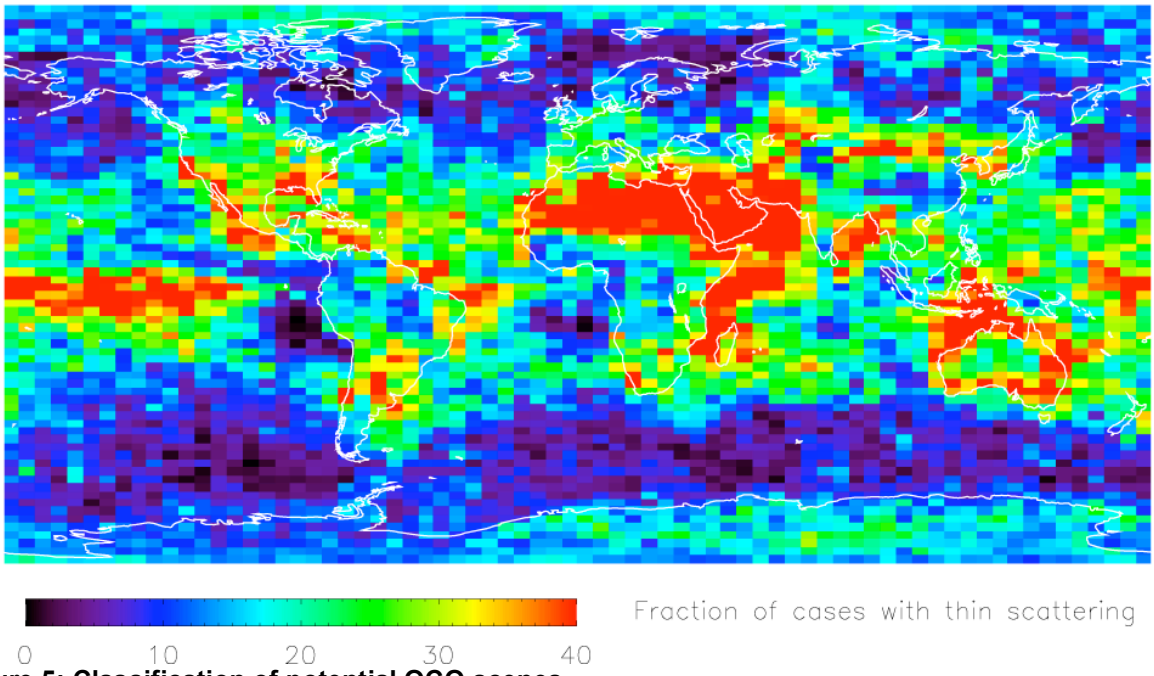

Figure 5: Classification of potential OCO scenes

It should be possible to process totally clear cases with a fast, low-cost algorithm. Because the almost clear cases only double the data density in regions already sampled by the totally clear cases, but do not extend the geographical coverage significantly, a question that must be addressed by the CO community is whether or not the science objectives of OCO can be met by processing only the totally clear cases. If so, then all the totally clear cases should be processed, without the need for a focus data set. Otherwise, GLAS data indicates that priority should be given to scenes with only aerosol rather than cloud, because such scenes are more numerous and because cloud is likely to introduce larger bias. Thus, analysis of GLAS data on the spatial and vertical distribution of aerosol and cloud, defines clear priorities for the development of the OCO algorithm.

A manuscript describing this work is about to be submitted to GRL (Bréon, O'Brien, and Spinhirne, 2005).

2.2.5. OCO Scene Classification and Cloud Detection

The arguments above are predicated on the assumption that scenes may be classified (totally clear, almost clear) confidently and expeditiously using OCO spectra. In collaboration with colleagues in the Department of Computer Science at CSU, a neural network classifier was developed to identify scenes with cloud water and cloud ice below specified thresholds. Neural networks are optimized on a training set, and then a validation data set is used to select the ten most skillful networks to form a 'committee'. Simulated test data is submitted to the committee of neural networks, and the average of the ten committee members is taken as the decision of the committee. When the prototype committee is used to decide whether radiance spectra were generated from scenes with cloud water and cloud ice below specified thresholds, the fractions of 'true positives' and 'false negatives' are approximately 90% and 10%. While these results are marginal, there are many avenues for improvement, which are being explored presently. Extensions to include aerosol will be addressed over the next year.

This work was presented to the annual OCO science team meeting (O'Brien and Anderson, 2005).

2.2.6. Efficient Inversion Algorithm Development

While the impact of the proposed satellite measurements of is high, so too is the associated risk. Rather than the traditional approach of rigorous testing of a prototype in a research aircraft, NASA has preferred to rely principally upon numerical simulations and to a small extent upon experiments with an airborne high resolution spectrograph in the O A-band conducted by O'Brien, Mitchell, English, and Da Costa (1998).

Compounding the risk is the complexity of the inversion algorithms that presently are being considered. According to the current paradigm for OCO, the algorithm will recover not only the vertical profile of CO volume mixing ratio, but also the profiles of temperature, water vapor and four type of particulates (clouds or aerosols), wavelength dependent models of surface reflectance and surface pressure. With eleven layers in the profiles, there are currently 84 parameters to be determined from radiance spectra in three bands. While successful inversions of simulated data have been demonstrated by the OCO science team (Kuang, Margolis, Toon, Crisp, and Yung, 2002) and also by Christi and Stephens (2004) at CSU, the operation of the algorithms remains obscure, in the sense that clear linkages between features of the spectra and the desired physical parameters have not been identified. An impediment to extensive experimentation is the numerical cost of the the inversions, which is prohibitive on all but the fastest computers.

Against this background, Stephens, Kumer, Menzel, and O'Brien (2001) proposed to IPO of NPOESS the development of an airborne etalon spectrometer operating in the 1.6 μm band of CO and the 760 nm band of O. As part of the current study, O'Brien (2004) conducted an end-to-end numerical simulation of the airborne spectrometer, including the extremely difficult task of developing a prototype inversion algorithm for in realistic atmospheric scenarios using a radiative transfer model commensurate in complexity with the information content of the spectra. The prototype model has but three physical parameters, , the mean height of scattering in the atmosphere, and the relative strengths of radiance scattered in the atmosphere and radiance reflected at the surface. Despite its simplicity, the model appears to be sufficiently flexible to accommodate atmospheric

conditions with optically thin cloud. Inversion of the model to recover is trivial. Although many technical details remain open, this approach is a significant advance; it rests on clear physical principles and could be the basis of a fast operational algorithm.

A technical report has been submitted to NPOESS (O'Brien, 2004), and a journal paper will be prepared in the near future.

2.3. Potential Clearsky Bias in Measurement of CO_2 from Space

The research presented in this section was the basis for the M.S. Thesis by Kathy Corbin, and is about to be submitted to GRL.

Retrieval of atmospheric CO2 mixing ratio from spaceborne instruments will require clear-sky conditions, which could introduce sampling errors in tracer transport inversions if mixing ratios depend on the presence or absence of clouds. Systematic differences in atmospheric CO2 in clear vs cloudy conditions might be expected because of the dependence of the rate of photosynthesis on the flux and directional character of solar radiation. Recent literature shows that the net ecosystem exchange (NEE) of CO2 is strongest on slightly cloudy days, due to greater light-use efficiency for diffuse rather than direct beam radiation, which might be expected to lead to the lower than average CO2 mixing ratios on partly-cloudy days [e.g. Gu et al., 2002; Freedman et al., 2001; Hollinger et al., 1994]. Satellite retrievals of only clear pixels might therefore overestimate spatial or temporal averages of CO2 because they will not see favorable cloudy conditions. Alternatively, heavy overcast conditions are expected to suppress NEE due to strongly reduced radiation, and could lead to systematic underestimation from spaceborne measurements during the growing season. Differences in atmospheric mixing ratio arising from differences in NEE would depend on the spatial scale of the differences in radiative forcing: small-scale cloudy or clear patches would have less effect on concentrations than large-scale perturbations because of horizontal mixing by winds. In winter, since the vegetation is not actively photosynthesizing, the a priori expectation is that CO2 mixing ratio would not depend on cloud conditions. In addition to differences arising from biology, sampling errors could also be caused by advection associated with cloud cover. Clouds are frequently associated with fronts and changes of air masses; and atmospheric transport may be systematically different on clear versus cloudy days.

Systematic differences in atmospheric CO2 mixing ratio between (measured) clear and (unmeasured) cloudy conditions will constitute a sampling error in satellite CO2 products. This sampling error could potentially introduce a bias in tracer transport inversions, depending on the treatment of the observations in the models. This study investigates clear-sky errors using continuous measurements of CO2 mixing ratio from two tower sites over a period of several years.

2.3.1. 2. In-situ data for evaluation of clearsky bias

To investigate clear-sky errors in near-surface measurements, we analyzed continuous data at two towers: a tall television tower near Park Falls, WI (WLEF, 45.95° N, 90.27° W) and the Environmental Monitoring Site at Harvard Forest, located in north-central MA (HF, 42.54° N, 72.18° W). The WLEF tower is in a heavily forested zone of low relief, and mixed evergreen and deciduous forests dominate the area surrounding the tower [see Davis et al. (1997) and Davis et al. (2003) for a description of the site and

measurements]. The CO2 concentration is measured continuously at 396 m with two independent Licor CO2 gas analyzers. The concentration used in this study is the average between the two measurements. To reduce data gaps, a single analyzer is used when one has missing data. Photosynthetically-active radiation (PAR) is also measured at the WLEF site; and net ecosystem exchange of CO2 (NEE, defined as the net flux out of the ecosystem) has been computed using eddy covariance methods. The WLEF CO2 and PAR measurements are available from 1995 through 2003, and we used NEE measurements from 1997 through 2001. The HF tower is in a mixed hardwood and conifer forest. Groups from the Atmospheric Sciences Research Center and Harvard University have made nearly continuous atmospheric measurements of CO2 concentrations, CO concentrations, PAR, turbulent CO2 flux at 29 m, and the rate of change in canopy carbon storage below 29 m; and all these variables are available from 1993 through 2002 [citation?]. We calculated NEE at HF by subtracting the storage measurements from the turbulent CO2 flux.

We sampled the continuous record of near-surface CO2 at mid-day, corresponding to the planned overpass time of the OCO satellite. To estimate the sampling error that could be expected from clearsky-only satellite retrievals of CO2 mixing ratio, we analyzed two different time periods: instantaneous values sampled at 13:00 local time, and the average value measured from 11:00 until 16:00 (the mean of six instantaneous values). The first is intended to represent a "single nadir pixel" sampled by the OCO (the fine field of view was chosen to maximize the chances of "see between clouds"), and the second is intended to represent the average of a swath of retrievals across an atmospheric transport model grid cell, which will be the basis of inversion of satellite CO2 products. At a mean wind speed of 10 m s-1, a six-hour average is equivalent to a 216 km swath of retrievals and comparable to global transport model grid scale. We chose 11 AM as the start time as the boundary layer remains relatively deep and unchanged during this afternoon time-span, which helps reduce mixing effects that may alter the concentrations at the towers [Davis et al., 2003].

We estimated the average difference in CO2, NEE, and CO between clear and cloudy days by (1) creating clear-sky subsets of timeseries of each variable, (2) fitting separate analytical (harmonic) functions to the clearsky subset and to the entire timeseries, and (3) subtracting the two analytical functions to obtain a seasonal climatology of the clearsky difference in each variable. Clearsky subsets were defined by selecting the mid-day values of each variable for days on which measured PAR was greater than a threshold value defined by month for each site. The threshold PAR values were set by ranking measurements from all years at each site, then selecting the value corresponding to the percentage of clear days for each month at the nearest city recorded by the National Climatic Data Center (NCDC, citation?). Thus if a given site was characterized by NCDC as having 20% clear days in a given month, we used days with the 20% highest mid-day PAR values in our clear-sky subsets of each variable for that month. The NCDC monthly climatology of clear days is based on at least 40 years of data and is determined by human observers who categorize each daytime hour as clear if the average cloud cover was less than 30%. For WLEF, the nearest stations in the NCDC database are Green Bay, WI (232 km away); Duluth, MN (175 km); and Minneapolis/St. Paul, MN (262 km). We used an average of the monthly clear-sky days from all three stations. At HF, the closest station is Worcester, MA (45 km). In setting PAR thresholds

for the clearsky subsets, we decreased the reported percentages of clear days by 5% to ensure that we do not overestimate the clear-sky differences by inadvertently including partly cloudy days.

We separately fit seasonally-varying harmonic functions of each variable to the entire timeseries and to the clear-sky subset using a linear least squares method. In preparing the data, we removed data for February 29 and de-trended the CO2 concentration, and required both the variable being investigated and the PAR measurement to be valid at each hour. We found that two harmonics per year fit seasonal variations adequately, without introducing spurious noise. Differences between the harmonic fits to clear-sky subsets the corresponding complete dataset are presented below and interpreted as the seasonal sampling error expected to occur in an average year by a satellite which only observes the atmosphere in clear conditions. Results are presented separately for both the one-hour and six-hour mid-day periods, representing local-scale and model grid-scale clear-sky sampling errors, respectively.

2.3.2. Sampling error associated with clear sky

Sampling the CO2 concentration only on clear days resulted in underestimation of the mean mixing ratio at both towers at all times of year (Figure 6).

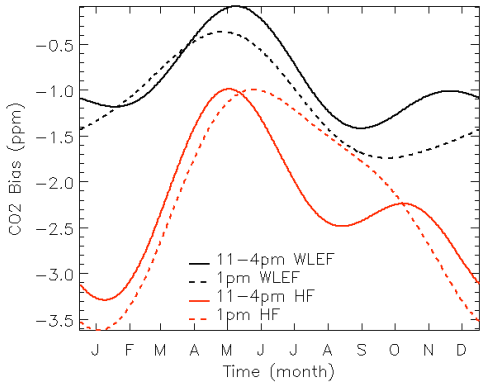

The seasonal cycle of the sampling error is similar for all four cases, with a greater near-surface difference in winter than during the summer months. The difference at the WLEF tower is smaller than at HF, which could reflect differences in vegetation, weather and climate, and/or transport. The seasonal cycle of the CO2 difference contradicts a priori expectations that the summertime sampling error would be positive due to the inability to see enhanced NEE on cloudy days and that the winter difference would be smaller. To investigate the mechanism controlling the relationship between observed CO2 mixing ratio and cloudiness, we analyzed differences in NEE and in the mixing ratio of CO.

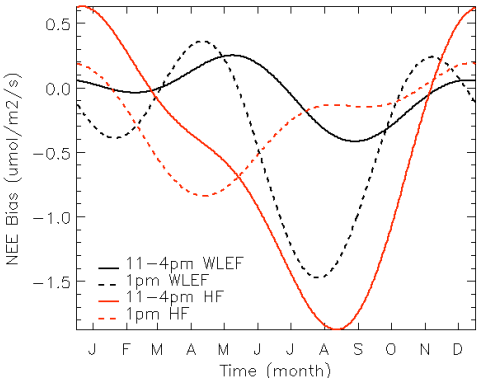

Clear-sky sampling error in mean NEE at both towers exhibit similar seasonal cycles (Figure 7), with a large negative difference in the summer indicating increased photosynthesis on clear days and a smaller bias in the winter (negligible at WLEF and slightly positive at HF). The negative summer sampling error, which is greater at HF corresponding to the larger CO2 bias, may be surprising in the context of recent observations of enhanced CO2 uptake on cloudy vs clear days (e.g., Gu et al, 2002). Previous studies investigated various levels of cloud cover to determine the optimal conditions for NEE, whereas we are comparing very clear days to all days. To better understand the nature of the clear-sky effect on NEE, we analyzed the mean seasonal cycle of NEE as sampled

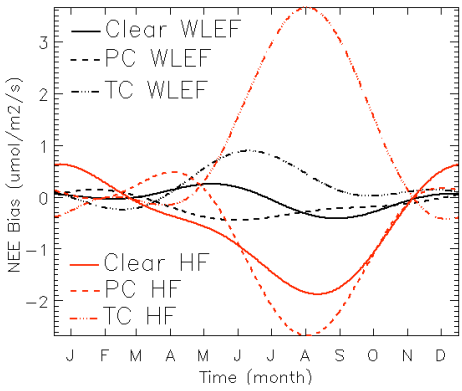

under a variety of different sky conditions. At both locations and for both times we calculated the NEE for partly cloudy days and for completely overcast days. We considered 25% of the days to be partly cloudy, using the days with the next highest PAR measurements below the clear-sky days, and we considered 40% of the days to be overcast, using the days with the lowest PAR values. We compared each of these subsets to the total time-series to determine the bias from the associated sky conditions. On partly cloudy days the NEE is indeed enhanced (Figure 8), showing a larger difference from all days in the summertime than the clear-sky subset. On overcast days during the summer, photosynthesis is reduced due to light limitation, causing a strong positive sampling difference. Although clear days do not have the strongest NEE, the clear-sky sampling error indicates that at these towers photosynthesis is more active on clear days than it is on average for all days, because reduced photosynthesis on overcast days overcomes enhanced photosynthesis on partly cloudy days.

Enhanced NEE on very clear days can evidently explain some degree of the reduced CO2 mixing ratio on clear days in the summer months, but this mechanism cannot explain the observed greater clear-sky difference in CO2 in winter than in summer. One possible explanation for the substantially lower CO2 observed on clear winter days (especially at HF) is a weaker contribution of anthropogenic CO2 on sunny winter days, either due to reduced emissions or deeper mixing. We calculated the clear-sky sampling effect on the mixing ratio of CO at HF to investigate the contributions of anthropogenic sources of CO2. Since CO is a ubiquitous by-product of the same combustion processes as CO2 and has an average lifetime of three months, CO measurements can provide information on the impact of combustion on CO2 [e.g. Bakwin et al., 2004; Suntharalingam et al., 2004]. Mid-day CO mixing ratio is lower on clear days for both sampling periods (Figure 9), indicating that the contribution of fossil fuel combustion is less. Like the CO2 differences, the clear-sky CO effect is stronger in winter weaker in summer, resulting from some combination of reduced combustion, deeper mixing, or differential advection on clear vs all days. Whatever the mechanism, it is clear that part (but not all) of the clearsky CO2 effect at HF is due to a smaller anthropogenic contribution on clear days, especially in winter. Assuming an average the combustion efficiency of 95%, which is consistent with both inventory estimates and atmospheric data [Bakwin et al., 2004, Miller et al., 2003], 40 ppb of CO corresponds to 1 ppm of CO2. Using these assumptions, the clear-sky sampling error for [CO] can explain an associated CO2 difference at HF of ~ -0.5 ppm in the summer and ~ -1.2 ppm in the winter.

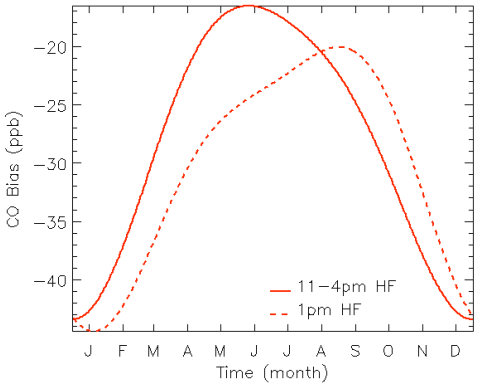

2.3.3. Explanatory Hypothesis

We propose that a combination of vertical mixing and advection are contributing to the clear-sky CO2 bias seen in the near-surface observations: the year-round negative clear-sky bias seen in both the CO and CO2 concentrations suggest that the boundary layer is deeper on clear days diluting the surface concentrations or that clear days are characterized by less advection of high CO2 concentrations from both natural and anthropogenic sources. To separate the relative contributions from vertical mixing and advection, we used a simple 1-dimensional "box" model to estimate the expected clear-sky difference in the mixing ratio of CO2 that would result from the observed difference in NEE. We specified the depth of vertical mixing using analyzed boundary layer heights from the European Centre for Medium-Range Weather Forecasts (ECMWF) 40-year Re-Analysis (ERA-40), using the depths from the grid cells that included the towers. We used the same procedure to calculate the clear-sky difference in boundary layer depth as described above for CO2, CO, and NEE. Since ERA-40 only reports mixing depth every six hours, the depths at 18 UTC are used at both 11-4 PM and 1 PM, making the clear-sky subset (consisting of the clear days from our CO2 analysis) the only difference between these two times. The primary feature in the data is the seasonal cycle of deeper boundary layers during the summer and shallower boundary layers in the winter (Figure 10). The summer boundary layer is deeper on clear days; however, during the winter the difference is not significant, and mixing is actually slightly shallower on clear days.

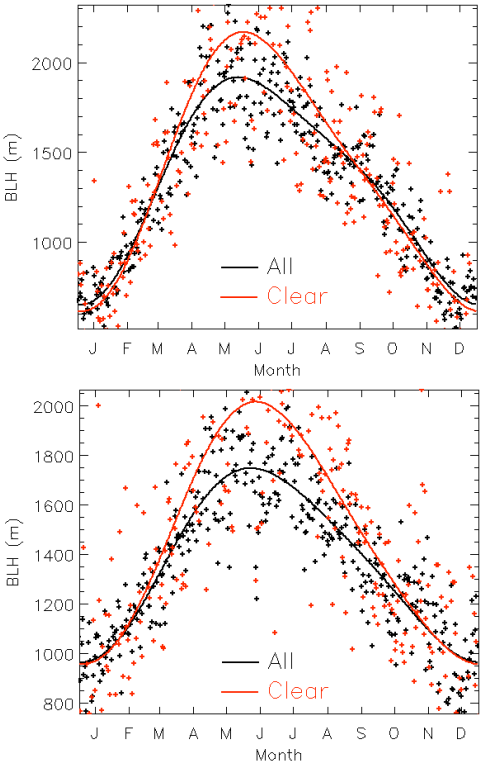

We calculated a winter and summer estimate of the clear-sky CO2 bias from enhanced vertical mixing using a simple box model. From the background concentration of 360 ppm in a 1 m2 box with a depth equal to the mean boundary layer height for all days and for clear-sky conditions in January and July, we added an average daytime value of NEE to the box. The winter and summer total NEE contribution for January and July is the corresponding average daytime NEE flux at each tower, and the clear-sky NEE flux estimates are the total NEE plus the mean NEE bias at each tower. The fluxes are multiplied by ten hours, which approximates the length of time plants are photosynthesizing and acting on an air mass. The new carbon concentration inside the box indicates the change caused by the local flux of carbon, and the bias seen at the tower from enhanced mixing and altered photosynthesis combined is the concentration in the clear-sky box minus the total box concentration calculated for both January and July. The resulting CO2 biases from biology and vertical mixing are –0.2 ppm and 0.07 ppm in the summer and 0.01 ppm and 0.2 ppm in the winter at WLEF and HF, respectively. In the summertime the bias appears smaller than expected because the deeper boundary layer is canceling the effect of the larger flux on clear days. The negative NEE bias seen in the observations depletes the CO2 concentration while the deeper boundary layer increases

low CO2, as it has to be mixed into a larger volume. The biases are also small in the winter, which is not surprising since the boundary layer depth and the NEE are nearly the same on clear days as they are on average. In this case, the box model illustrates that the large winter bias is probably not due to the vegetation or vertical mixing, but instead is likely due to advection.

Since the bias from vertical mixing of the CO2 vegetation flux is small, especially in the winter, we can assume that the negative CO2 bias must be due to less advection of high CO2 concentrations on clear days. From the CO bias we know that advection of fossils fuels is contributing substantially to the negative CO2 bias; however, this bias alone is not sufficient to create the large biases seen in the observations during the winter. The last factor that is contributing to the negative CO2 bias is less advection of high CO2 from natural sources or more advection of low CO2 from natural sinks or across regional CO2 gradients. Although we cannot calculate this contribution from point data, it is certainly possible that this factor could cause the remaining unexplained biases. On clear days, the air being advected over the tower could have lower CO2 than average due to the accumulation of low CO2 from enhanced photosynthesis or due to a different source region of air. Fronts and synoptic scale disturbances, which are associated with clouds, could contain air with higher CO2 concentrations from a different region than the source region for clear days, and the negative bias could be due to under-sampling these events.

2.4. Sampling and representation error at regional synoptic scale

This section describes portions of the M.S. Thesis of Kathy Corbin, and is about to be submitted to JGR-Atmospheres

The X_{CO2} fields retrieved by OCO will be used as inputs to synthesis inversion and data assimilation models. The concentrations from OCO have the potential to help reduce the uncertainty in the flux estimates from inverse models; however, to utilize X_{CO2} measurements, inversion models and data assimilation systems must correctly account for several types of sampling errors: spatial representativeness errors may be introduced into inversions that compare CO2 concentrations from a model grid cell to satellite concentrations sampled over only a fraction of the domain, temporal sampling errors can result from comparing OCO measurements sampled at 1:15 PM to temporally averaged concentrations in an inversion, and local clear-sky errors may exist in inversions that compare concentrations in a grid cell that may be partially cloudy to satellite mixing ratios sampled at the same time but only over clear areas. Since incorrectly accounting for these sampling errors could lead to incorrect inversion results, this study investigates these spatial, temporal, and clear-sky errors using a high-resolution, coupled ecosystem-atmosphere model, SIB2-RAMS.

2.4.1. Model Description, SiB2-RAMS

The biosphere model used in this study is the Simple Biosphere Model, SiB2 [Sellers et al., 1986; Sellers et al. 1996a,b; Denning et al., 2003]. SiB2 calculates the transfer of energy, mass, and momentum between the atmosphere and the vegetated surface of the earth. SiB2 has a single vegetation canopy layer that is represented by one of thirteen cover types or biomes and three soil layers, where the soil texture is one of twelve categories based on the soil properties within the United States Department of Agriculture (USDA) texture classes. To describe the interception, reflection,

transmission, and absorption of radiation by vegetation and soil, SiB2 uses the two-stream approximation originally described by Coakley and Chylek [1975] and extended by Sellers [1985]. Fluxes of water vapor, sensible heat, and CO2 are expressed as differences in potentials divided by resistances [Sellers et al., 1997]. The photosynthesis model of Farquhar et al. [1980] and the stomatal model of Ball [1988], which was expanded by Collatz et al. [1991,1992], are the basis for the photosynthesis-conductance model in SiB2, and photosynthesis and conductance are explicitly connected by the Ball-Berry relationship. The individual leaf assimilation and stomatal conductance is scaled up to canopy photosynthesis using Beer's Law for interception and absorption of PAR. SiB2 is a balanced model, with the respiration over a year equaling the assimilation in that year.

The meteorological model coupled to SiB2 is the Brazilian version of the CSU Regional Atmospheric Modeling System (RAMS). RAMS is a comprehensive mesoscale meteorological modeling system designed to simulate atmospheric circulations spanning in scale from hemispheric scales down to large eddy simulations of the planetary boundary layer and is discussed in detail by Pielke et al. [1992] and Cotton et al. [2002].

A significant feature of RAMS is the incorporation of a telescoping nested-grid scheme, which allows the model to solve the equations simultaneously on any number of interacting computational meshes of differing spatial resolution. The turbulence closure option used is the Mellor Yamada [1982] scheme for vertical diffusion and the Smagorinsky [1963] scheme for horizontal diffusion. A combination of the Grell parameterization scheme and the RAMS microphysics scheme was used in this study: the coarse domains used the Grell convective cumulus scheme, which is an entraining plume model based on the quasi-equilibrium assumption [Grell, 1993; Grell and Devenyi, 2002] and the finer resolution domains are intended to represent cloud processes explicitly using the bulk microphysics parameterization in RAMS. Details of the microphysical parameterization are presented in Meyers et al. [1997] and Walko et al. [1995]. This study uses the two-stream radiation scheme developed by Harrington [Harrington, 1997; Harrington et al., 1999], and the radiation condition discussed by Klemp and Wilhelmson [1978] is used at the lateral boundaries, which assumes that disturbances reaching the boundaries move as linearly propagating gravity waves and is intended to allow most disturbances to propagate out of the model domain without strongly reflecting back to the interior [Walko and Tremback, 2002]. Additionally, this simulation utilized analysis nudging by Newtonian relaxation that is implemented in RAMS, in which the model fields on the lateral boundaries can be nudged toward observational data as the simulation progresses.

The vegetation in SiB2-RAMS is the 1-km land cover classification data derived from AVHRR at the University of Maryland, which is described in Hansen et al. [1998, 2000]. These classes have been converted to SiB classes to make the data compatible with SiB2-RAMS. The soil data used in this study was generated by the SoilData System, which was developed by the Global Soil Data Task Group of the International Geosphere-Biosphere Programme (IGBP) Data Information System, and it is available on CD-ROM from the Oak Ridge National Laboratory Distributed Active Archive Center in Oak Ridge, TN (Global Soil Data Task, 2000). The original data was a 5' x 5' (~10 x 10 km) resolution map containing values of % sand, % clay, and % silt. Using a

triangulation program, the data was converted to SiB soil classes and then masked to the vegetation map to ensure the maps agree on the location of water pixels. If the vegetation map had water in a pixel that did not originally correspond to a water pixel in the soil map, then the soil pixel was set to water. In contrast, if the biome map had a vegetation class and the soil type was water, then that pixel was set to the nearest soil class. This study uses 1 km resolution SPOT 10-day composited Normalized Difference Vegetation Index (NDVI) from the United States Department of Agriculture Foreign Agriculture Service (USDA/FAS) through collaboration with the Global Inventory Modeling and Mapping Studies (GIMMS) Group at NASA/GSFC. The SPOT data is from the VEGETATION instrument on board the SPOT-4 polar orbiting satellite.

To prepare the NDVI data for SiB2-RAMS, the data went through several processing steps. First, the data were filled using status maps also provided by USDA/FAS, which indicate whether the datum at each pixel is valid or contains errors. Since the northern portion of North America does not receive any solar radiation during the winter, SPOT is unable to retrieve NDVI values in the high latitudes during the winter months. To fix this, the missing NDVI pixels were filled by linearly interpolating the values at the same pixel between the last value SPOT retrieved in the fall and the first value it retrieved for that pixel in the spring. In addition, all points where the status map indicate that either the ground was covered with ice/snow or that the area was covered by clouds during the 10-day period were also filled by interpolating the closest values in time at that pixel. Since the NDVI maps were provided in Mercator projection, they were re-projected into latitude and longitude coordinates. Finally, the NDVI data were masked to the vegetation map from the University of Maryland. Similar to the soil map, any pixel that was water in the vegetation map was required to be water in the NDVI maps and any pixel that had a vegetation class other than water but was considered water in the original NDVI map was assigned a non-zero NDVI by interpolating the NDVI values from the nearest pixels.

Surface fluxes of carbon to the atmosphere due to fossil fuel combustion, cement production, and gas flaring were derived from the 1995 CO2 emission estimates of Brenkert [1998]. The data was obtained from the Carbon Dioxide Information Analysis Center (CDIAC) at the Oak Ridge National Laboratory in Tennessee. Since the resolution of the data is one degree by one degree, the fossil fuel fluxes are interpolated to the finer resolutions used in this study. The 1995 carbon emissions estimates were converted to carbon fluxes in units of kgC/m2/s, and the surface flux was scaled from the annual 1995 estimates to estimates for August 2001 by multiplying the surface fluxes by a scaling factor of 1.124, which was calculated using monthly estimates of global anthropogenic emissions (A. Wang, personal communication).

To spin-up the soil moisture and the soil respiration factor, SiB was run offline from 1991 through 2001 with 1º x 1º resolution. The soil moisture in SiB2-RAMS is initialized from the soil moisture fields produced by offline SiB driven from NCEP re-analysis. For grids in SiB2-RAMS with a smaller resolution than the offline model, if the grid cell in SiB2-RAMS has the same biome type as the offline SiB cell or any immediately adjacent pixels, then the grid cell of SiB2-RAMS has the same respiration factor as the offline SiB cell with the same biome class. If the SiB2-RAMS biome type does not match either the SiB cell it resides in or the adjacent cells, then the SiB2-RAMS

respiration factor is set to the biome-based global average respiration factor (A. Wang, personal communication).

The meteorological fields in SiB2-RAMS are initialized using the National Center for Environmental Prediction (NCEP) mesoscale Eta–212 grid analysis (AWIPS 40-km). The Eta-212 analysis covers most of North America, has 40-km horizontal resolution, and three-dimensional output that is provided on about 25 constant pressure surfaces spanning from 1000 mb to 25 mb at intervals of 50 mb. In addition to using the Eta-212 data for initial conditions, the lateral boundaries are nudged towards the 3-hourly Eta analysis. The CO2 field in SiB2-RAMS is initialized to 370 ppm, and the lateral boundaries are also set to 370 ppm in this study.

2.4.2. Case Description

We will analyze a ten-day simulation centered on the WLEF tall tower in Wisconsin (45.95° N, 90.27° W). The case has a coarse domain and three nested grids, which are displayed in Figure 11. The top panel shows the coarse domain, with the size and placement of the three nested grids outlined in red. The bottom two panels show the vegetation classification for grids 3 (left) and 4 (right). Grid 3 includes part of Lake Superior. The upper and middle portions of the domain are dominated by mixed forest, while the southern third contains significant areas of agriculture and cropland. Zooming in to grid 4, the vegetation is primarily mixed forest and broadleaf deciduous trees with a few patches of evergreen trees and agriculture. Grid 4 contains several small lakes, with a relatively significantly sized lake just north of the WLEF tower. In this study, we will analyze both grid 4, which we will call the fine grid, and grid 3, which will be called the coarse grid. The fine grid has a grid increment of 1 km and is 97 km x 97 km and the coarse grid has a 5 km resolution and covers 450 km x 450 km.

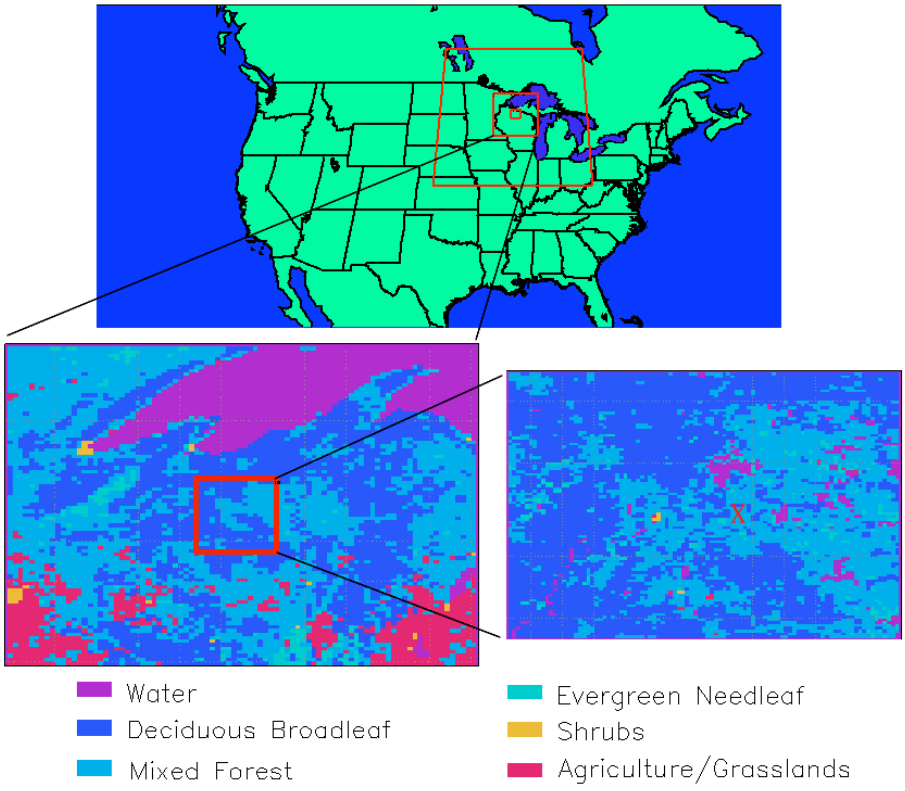

This case simulates twenty days, from 00 GMT August 1 to 00 GMT August 21, 2001, but the first ten days are used to spin-up the model. The time period we will analyze from this simulation is from 00 GMT August 11 to 00 GMT August 21. During

this ten-day time period, three fronts passed over the WLEF tower. The simulation began with mild weather: the temperature was moderately warm and the wind was light and predominantly from the southwest. The pressure began to drop the night of August 11, and the first simulated front passed over the WLEF tower at 02 LST on August 12, with winds shifting counterclockwise to northerly. Following the front, the wind speed decreased but the wind remained out of the north. The 13th is a typical clear summer day: the temperature is moderate with a light wind while the pressure increased. That evening, the wind shifted directions and again became southwesterly. The night of August 14th, the surface pressure began to drop and the southwesterly wind strengthened. The pressure continues to drop during the day on the 15th as the wind shifts again to northerly, and the second front passes over the WLEF tower at 23 LST the night of the 15th. Early morning on the 16th the wind began to relax and shift to the west while the pressure increased. The morning of the 17th the pressure again began to decrease as the wind once more shifted to northerly, bringing the third front at 18 LST on the 17th. While the pressure increased on the 18th, a strong northeasterly wind continued and the temperatures were much warmer than the previous few days. On the 19th, the wind speed decreased and began its clockwise shift from the north through easterly to southwesterly as the temperature and pressure both increased. The 20th continued the moderate weather conditions seen on the 19th, with an increasing surface pressure, warm temperatures, and a light wind from the southwest.

2.4.3. Simulating OCO Using SiB2-RAMS Output

Since OCO will estimate total column CO2 concentrations, the mixing ratios from the model are vertically integrated by pressure weighting. Since the vertical coordinate of the model output is height, we will use a standard atmosphere to find the corresponding pressure, which is then used to weight the CO2: the concentration at each height is multiplied by the difference in pressure between the upper and lower boundaries surrounding the current level. The values are then summed and divided by the sum of the pressure changes, yielding the CO2 concentration for the entire vertical column of air.

After computing the total column CO2, we had to imitate a satellite track. For simplicity, we assume that the satellite travels due south and that all the footprints over the different latitudes sampled within the domain will be averaged together to yield only one concentration for the grid. To emulate this spatial averaging in the satellite measurements, we averaged all the latitudinal values together to produce one CO2 concentration for each longitude. The width of the emulated satellite track is 10 km. For the fine grid, a single satellite measurement from one track is the mean of ten 1-km grid cells, or pixels, in the x-direction and all the pixels (97) in the y-direction. The fine domain has 88 different possible satellite tracks at any one point in time. Similarly, for a satellite measurement in the coarse grid is the mean of two 5-km pixels in the x-direction and all the pixels (90) in the y-direction, with 89 different possible satellite tracks.

2.4.4. Simulated Cloud Cover

Since satellites will not be able to measure the CO2 concentration under cloud cover, we need to identify the cloudy pixels in the simulation. A single pixel was considered cloudy if any vertical level in the atmosphere had a cloud mixing ratio, which included liquid water and ice condensates, greater than 1.e-6 g/kg. Maps of the daily

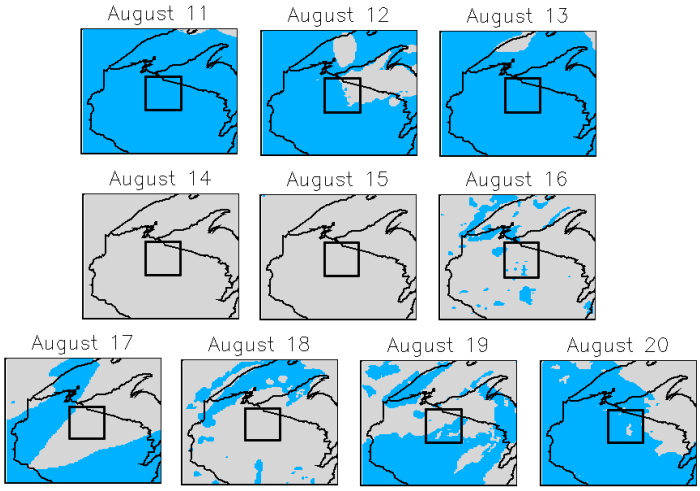

cloud cover at 1 PM are shown in Figure 12, where blue indicates the sky is clear and gray indicates the pixel is considered cloudy. The coarse domain is shown and the fine domain is the region inside the inner black square. During the ten-day simulation, two days are mostly clear, five days are partly cloudy, one day is primarily cloudy, and one day is completely cloudy. On August 11, 12, and 13, the small clouds on the northern portion of the grid are probably cumulous clouds, as a vertical profile of the cloud mixing ratio indicates that the clouds exist approximately 2 to 3 km above the ground. August 14 is primarily covered by thin cirrus 6 to 14 km above the surface that allow the majority of the short-wave radiation to pass through. August 15 has a few clear pixels in the northwestern corner but is primarily cloudy with condensates apparent throughout the entire vertical profile that significantly lower the incoming radiation. On August 16, the cloud cover appears to be breaking up, with many clear patches through the low-level, thick clouds. Looking at August 17, 18, and 19, the clouds are patchy and exist from near the surface up to approximately 15 km. Finally, on August 20 the sky is still only partly cloudy with cumulus clouds 1 to 2 km above the surface.

2.4.5. Total Column CO2 Concentrations

Daily spatial maps of total column CO2 concentrations with overlaying 30 m wind vectors at 1 PM are shown in Figure 13, displaying the spatial variability that a single satellite track must represent. At 1 PM, the daily variability of total column CO2

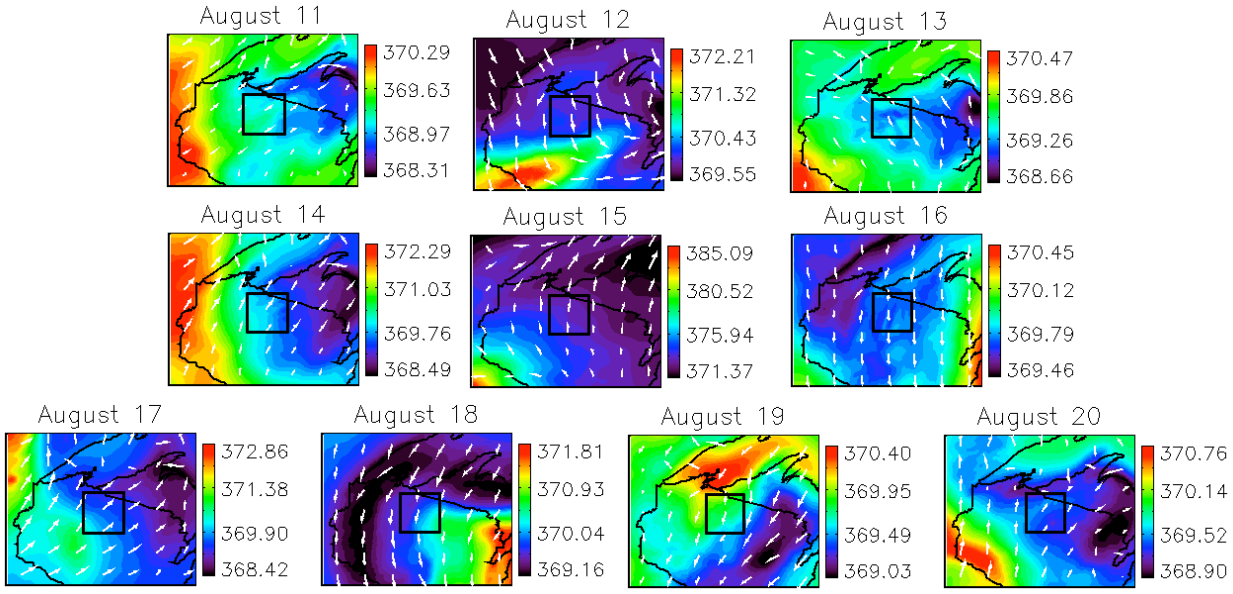

concentrations in the fine domain ranges from 0.2 to 1.8 ppm, with an average variability

of 0.8 ppm on this domain. In the fine grid, the CO2 spatial patterns do not resemble the cloud cover maps, indicating that the main driver to the spatial variability is advection. The daily total column CO2 variability at 1 PM in the coarse grid is considerably larger, ranging from 1 ppm to 13.7 ppm. These patterns in CO2 are influenced both by advection and photosynthesis, as regions with increased concentrations due to the reduced radiation limiting photosynthesis can be seen. The heterogeneity of the domain and the combination of Lake Superior and the land also contribute to the larger spatial variability on the coarse domain.

Looking at the day-to-day variability, the modeled total column CO2 concentration at the WLEF tower for our ten-day simulation is shown in Figure 14, which also shows the modeled cloud cover. The red line shows the CO2 concentrations, which are in ppm. The cloud cover is displayed in the black line, with 0 representing clear skies and 1 representing clouds. Rather than following a diurnal cycle, the figure shows that the CO2 concentrations are higher on cloudy days than on clear or partly cloudy days, with the three spikes in the CO2 concentrations coincide with the timing of the three fronts. The fronts advect higher CO2 from the southwest, as a heat wave and drought in Texas and Oklahoma cause respiration anomalies that are advected up to the WLEF tower by the frontal passages. In contrast, the lowest concentrations seen in the simulation occur when the sky is clear. In general, the variability from weather is greater than the spatial variability due to the heterogeneity in land cover, indicating that advection and synoptic scale conditions cause the greatest CO2 changes.

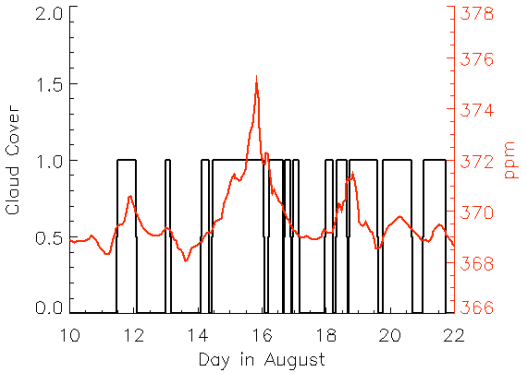

2.4.6. Spatial Representativeness Errors

Satellite measurements can be used in inverse models; however, the width of the satellite track is not the same as the size of the grid cell in an inverse model. If the inverse model optimizes the concentrations in an entire grid cell to satellite concentrations from only a small fraction of the domain, errors may be introduced into the inversion as the satellite mixing ratios may not be representative of the entire grid cell. To calculate the spatial representativeness errors, we subtracted the domain-averaged concentration at 1 PM from each simulated satellite concentration using only clear-sky pixels.

Figure 15 displays the compiled representativeness errors at 1 PM from all ten days of the simulation. The left panel of the figure displays the results from the fine grid, and the right panel shows the sampling distribution of the errors from the coarse domain.

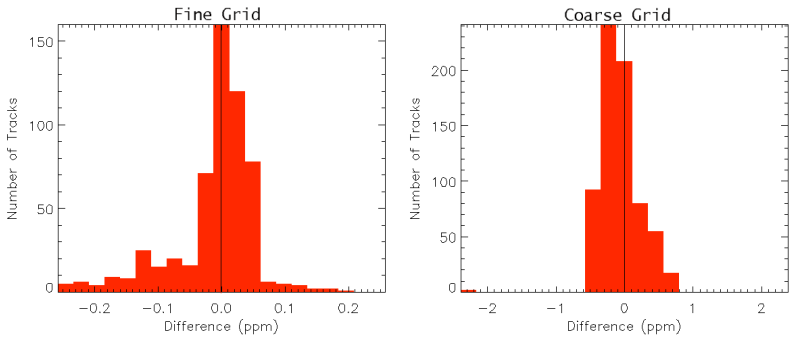

In the fine domain, all of the emulated satellite values are within 0.26 ppm of the domain mean and 95% of the satellite tracks have a spatial error of less than 0.2 ppm. The small magnitude of the error is not too surprising, since the variability at 1 PM was on average only 0.8 ppm. The distribution of this error is nearly gaussian, indicating that the small spatial errors are not biased.

On the coarse domain, the range of errors is considerably larger, primarily because the greater daily CO2 variability on this grid, which averaged 3.5 ppm. Similar to the fine grid, the distribution of the errors is relatively symmetrical. Over 99% of the tracks have a spatial error less than 0.8 ppm, but two tracks underestimate the domain-average concentration by more than 2 ppm. The largest errors came from the two tracks that had clear pixels on August 15, when the emulated satellite concentrations underestimated the mean concentration by more than 2 ppm. These two concentrations are from a few pixels of clear sky in the far northwestern corner. The large errors occur because the northwestern corner had the lowest concentrations in a gradient of nearly 15 ppm in total column CO2. Our study demonstrates that large errors are possible when looking through small holes in the clouds and then using the measurements to represent a large area, but the number of tracks with an error more than 1 ppm is less than 1%.

2.4.7. Temporal Representation Errors

Next we will investigate the errors from using clear-sky measurements to represent the mean concentration over the entire simulation, which is analogous to comparing the clear-sky total column OCO concentrations to diurnal, weekly or bimonthly CO2 averages in inverse models. We are calling these errors temporal sampling errors because OCO will never be able to sample the concentrations on cloudy days. To calculate the clear-sky errors from sampling only clear days compared to the temporal average, we subtracted the mean domain concentration over the entire 10-day simulation from each clear-sky emulated satellite track at 1 PM.

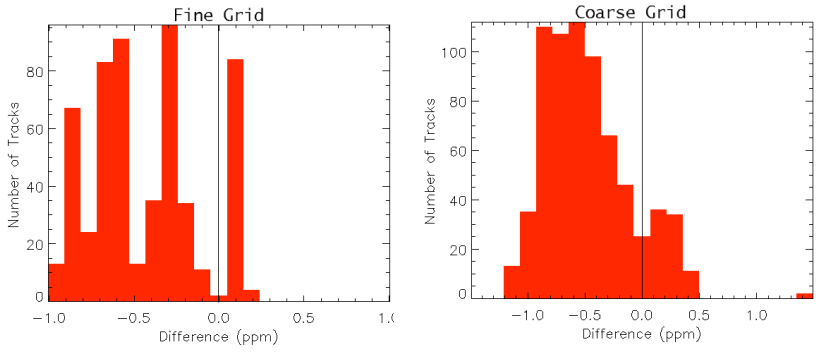

The compiled sampling distribution of temporal sampling errors is shown in Figure 16. The majority of the satellite tracks from both domains underestimate the 10-day domain mean, illustrating that temporal averaging will introduce large errors and may have a negative bias. Looking at the fine grid, each peak in the sampling distribution is a different day, again indicating that the day-to-day variability of CO2 is much greater than the spatial variability. The days that are primarily clear, particularly August 11 and 13, have the largest errors; and in general, the greater the fraction of clear sky the larger the underestimation of the temporal mean. The days following fronts typically have smaller errors because the concentration has not yet been depleted by photosynthesis.

On the coarse domain, the majority of the satellite tracks underestimate the 10-day domain average, although a few tracks grossly overestimate the mean. The large overestimation of the temporal mean is caused by the two satellite tracks on the 15th that each have a few clear pixels. Due to the front advecting in high concentrations at 1 PM, the clear tracks overestimate the temporal mean. The large and biased errors seen in Figure 16 indicate that using clear-sky concentrations to represent a temporal average may introduce large errors or even a bias at some locations.

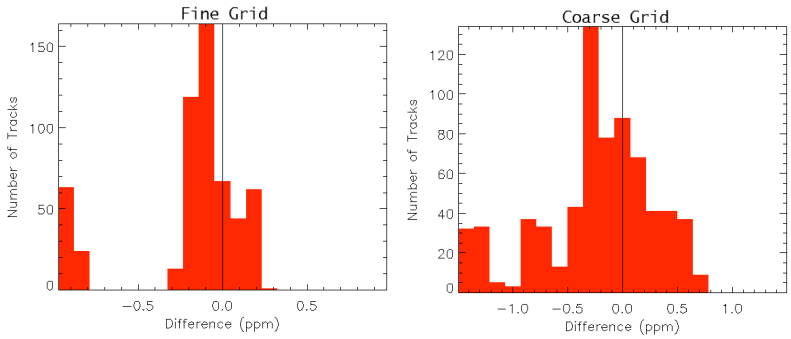

We also analyzed the temporal sampling errors from comparing satellite concentrations to the diurnal mean, which is shown in Figure 17. To calculate these errors, we subtracted the mean 6 to 6 PM diurnal concentration over the entire domain from each clear-sky emulated satellite track at 1 PM. On the fine grid, ~30% of the tracks overestimated or equaled the diurnal mean and ~60% underestimated the mean, with nearly 20% of the tracks underestimating the diurnal mean by more than 0.9 ppm. The large underestimations of the diurnal mean occurred on August 16th, when all of the tracks underestimate the mean by at least 0.8 ppm. Since the second front passed over ~11 PM on the 15th and had high concentrations, the increased CO2 is included in the diurnal mean for the 16th. Although the concentrations dropped rapidly early morning on the 16th, the inclusion of the high concentrations the night of the 15th raised the diurnal mean and made the concentrations at 1 PM appear to badly underestimate the diurnal mean.

The shape of the distribution in the coarse domain is similar to the fine domain, as the largest number of tracks slightly underestimate the diurnal mean by ~0.3 ppm; however, the magnitude of the errors is greater. The tracks that overestimate the concentration have errors up to 0.65 ppm and the emulated satellite concentrations that underestimate the diurnal mean have errors as large as 1.5 ppm. As we saw in the spatial representativeness errors, the larger domain has greater errors due to the enhanced total column variability in CO2. For both domains, the main determination of the temporal representation errors is synoptic events, suggesting that satellite measurements will not capture frontal samples and will create large sampling errors if used to represent temporal averages. To avoid incorporating these large errors into inverse studies, inverse models must accurately model the synoptic-scale transport and not compare temporally averaged concentrations to satellite measurements taken at one point in time.

2.4.8. Locally-Forced Clear-Sky Errors

We calculated the local clear-sky total column CO2 errors for both domains, which are the errors introduced by using clear-sky satellite concentrations to represent a domain that includes clouds. For this calculation, we subtracted the emulated satellite

total column CO2 concentration at 1 PM using all pixels from the mixing ratios using only clear-sky pixels in the track at 1 PM.

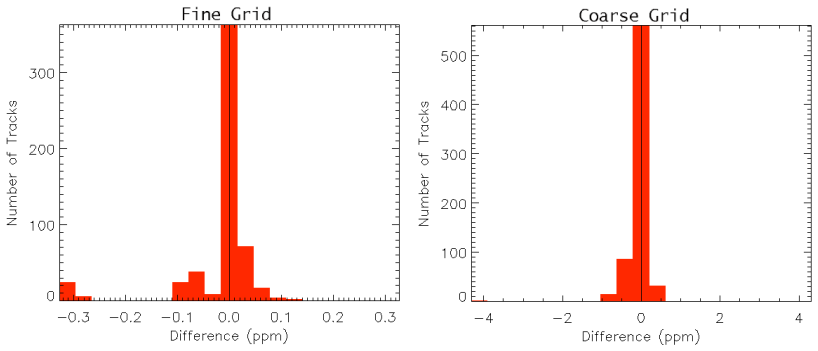

Figure 18 shows the local clear-sky errors. August 14 was completely cloudy and thus had no corresponding emulated satellite tracks. On the fine domain, the local clear-sky errors are quite small, with the largest error being –0.33 ppm. Nearly 60% of the satellite tracks do not have any clear-sky error, and as many tracks overestimate the concentration as underestimate the mean concentration. The range of errors becomes larger as the track samples fewer pixels due to clouds. This result is expected, as the satellite sees fewer pixels it becomes more difficult to capture the mean concentration. The largest local clear-sky errors on the fine domain occurred on the 17th. Looking back at the cloud cover maps, the majority of the tracks were covered by cloud, and the clear portion of the domain, which was the northwest corner, had relatively low concentrations with a strong gradient to high CO2 in the southwestern corner. Since the tracks could not see the high CO2 being advected into the southwest corner, they underestimated the concentration.

In the right panel of Figure 18, the majority of the clear-sky errors on the coarse grid are larger; however, the error in 80% of the tracks is still less than 0.3 ppm. Although more tracks underestimate the mean, the local clear-sky CO2 errors are not biased like the temporal sampling errors, with a substantial percentage of tracks overestimating the mean. Two tracks grossly underestimate the concentration by over 4 ppm in the total column. The large clear-sky errors come from August 15th, the day that also had large spatial and temporal errors. The two tracks with very few clear pixels drastically underestimate the mean concentration in the track because high CO2, with a large gradient, is being advected into the domain prior to the front but has not yet reached the clear pixels in the northwest corner.

The dominant source of error encountered in these high-resolution simulations of was temporal sampling errors, which are errors that can be introduced into an inversion if the model uses satellite concentrations only in clear columns at 1:15 PM to optimize temporally averaged concentrations. The main driver of the total column CO2 variability is not the diurnal cycle of CO2 from biology, but instead is synoptic variability. In Wisconsin, temporal sampling errors from under-sampling fronts associated with clouds and high CO2 caused a bias of ~-0.5 ppm compared to the domain-averaged ten-day mean. Although this negative bias occurred at a specific location during a ten-day period that included three fronts, one of which had an unusually large CO2 concentration anomaly, the large variability of total column CO2 concentrations associated with synoptic events indicates that satellites will not be able to represent a temporal average. To avoid these errors, inverse models will have to accurately model the synoptic-scale

atmospheric transport, and inversions will have to use the measured satellite mixing ratios to optimize modeled concentrations sampled at the same time.

Both the spatial errors and local clear-sky errors are primarily smaller than the 0.5% instrumental error; however, the precision of the measurement depended on the size and the heterogeneity of the domain the measurements are representing. In a relatively homogeneous domain consisting of similar vegetation types, 95% of the spatial and local clear-sky errors are <0.2 ppm and are normally distributed. The errors are small for a 97 km x 97 km domain because the variability at 1 PM on that scale is limited, typically <1.0 ppm. The SiB2-RAMS simulations suggest that the errors in the total column concentration due to altered photosynthesis on cloudy vs. clear conditions are very small and that the local clear-sky errors are primarily due to advection rather than the biology. As the domain size and heterogeneity increases, the spatial variability in the domain increases. Looking at a relatively heterogeneous area in Wisconsin including portions of the Great Lakes, the spatial and local clear-sky errors both increased to a standard deviation of ~0.4 ppm. To prevent introducing spatial representation and local clear-sky errors, inverse models should obtain fluxes by optimizing concentrations over regions with relatively homogeneous vegetation coverage and by avoiding domains that include both water and land.

This study has investigated the spatial, diurnal, and clear-sky errors extensively in Wisconsin during the summer, using a time period that included three fronts with dramatic CO2 concentration anomalies. Although we investigated a relatively heterogeneous domain, the errors could be different over various regions. While it is likely that the spatial and local clear-sky errors will remain small except over exceptionally heterogeneous domains, they should be investigated at other locations, including regions that contain point sources. Since not all regions actively photosynthesize during the summer and since regions may be closer to anthropogenic sources, the temporal sampling errors will be different around the world and require further investigation. In addition to sampling alternate regions, different times of year also need to be investigated.

2.5. Transport model error

Given additional observing capabilities of the OCO era, a leading source of error in the source/sink retrieval problem is likely to be transport model error. Although exact knowledge of the error in atmospheric transport models is impossible, we have participated in well-organized international intercomparison of models currently in use for carbon source inversion (led by the PI of this project from 1995-2004). Given identical observations and inversion methods, the differences in source/sink retrieval among current transport models provides the best available measure of the effect of transport error on flux estimates. With support from NCC5-621, we investigated the effects of model transport error on the attribution of interannual variability in the carbon cycle to various regions and processes, and on the likely impact of model transport error on inversions of space-based measurements of the CO_2 mixing ratio.

2.5.1. Effect of Transport Error on Inversion of in-situ CO_2

This research is described in detail in a manuscript by Baker et al (2005, attached) which is accepted for publication in JGR.

Monthly CO2 fluxes are estimated across 1988–2003 for 22 emission regions using data from 78 CO2 measurement sites. The same inversion (method, priors, data) is performed with 13 different atmospheric transport models, and the spread in the results is taken as a measure of transport model error. Interannual variability (IAV) in the winds is not modeled, so any IAV in the measurements is attributed to IAV in the fluxes. When both this transport error and the random estimation errors are considered, the flux IAV obtained is statistically significant at $P \leq 0.05$ when the fluxes are grouped into land and ocean components for three broad latitude bands, but is much less so when grouped into continents and basins. The transport errors have the largest impact in the extra-tropical northern latitudes. A third of the 22 emission regions have significant IAV, including the Tropical East Pacific (with physically-plausible uptake/release across the 1997–2000 El Nino/La Nina) and Tropical Asia (with strong release in 1997/98 coinciding with large-scale fires there). Most of the global IAV is attributed robustly to the tropical/southern land biosphere, including both the large release during the 1997/98 El Nino and the post-Pinatubo uptake (Fig 19).

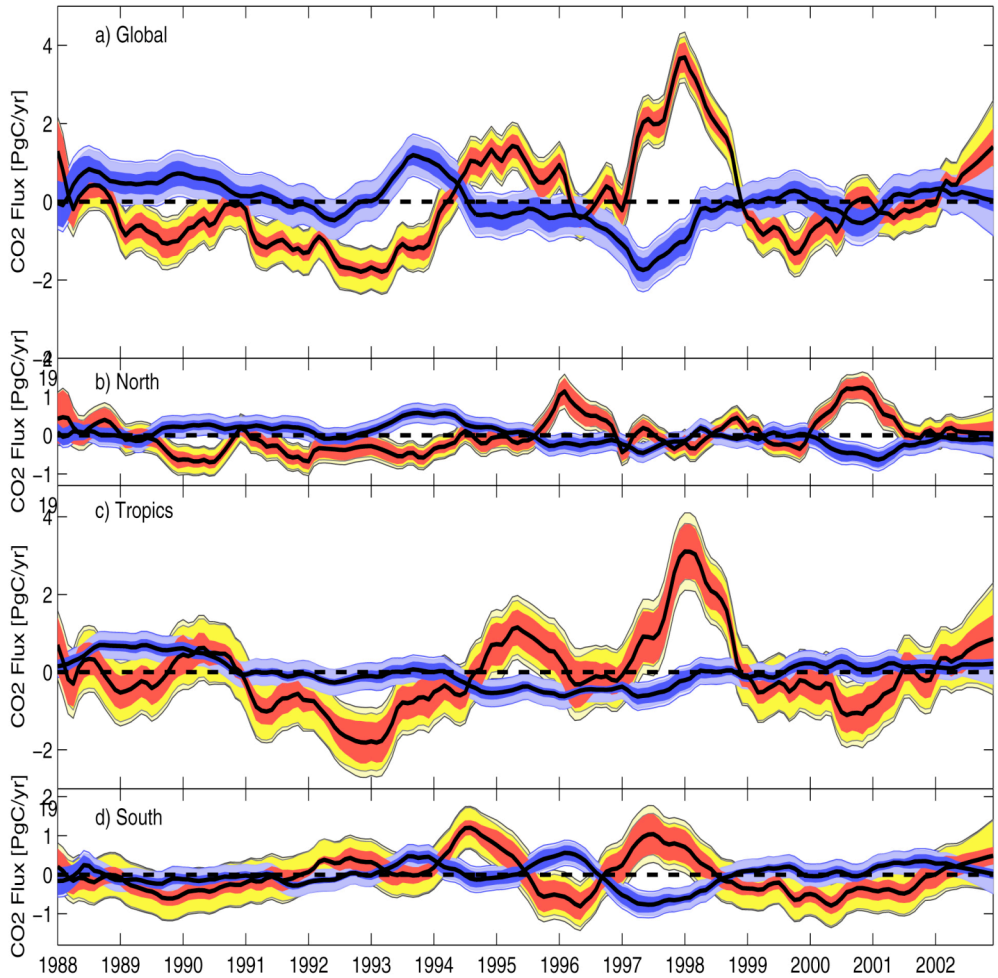

Figure 19: Interannual variations in land (red) and ocean (blue) carbon fluxes since 1988 as deduced from the TransCom intercomparison. The 13-model mean (black line) is bounded by the 1σ inter-model spread (dark shading), the 13-model RMS 1σ estimation uncertainty (light shading), and the RMS of the two (outer envelope).

2.5.2. Effect of model transport error on satellite inversions

The research described in this section is to be reported in a manuscript in preparation for JGR.

To investigate the effect of transport error on source inversions from satellite data, we used the monthly mean response functions for each of the thirteen transport models participating in TransCom to invert synthetic satellite retrievals made from one of the models. The synthetic data were built from the response functions of the CSU GCM to optimized fluxes based on a cyclostationary inversion of real (in-situ) observations. They therefore feature realistic seasonal and spatial variability at the locations of the NOAA flask stations (Gurney et al, 2004). These global 3D fields were then sampled and averaged in the vertical according to two vertical weighting functions: one weighted heavily toward the upper troposphere, representing thermal IR retrievals from AIRS spectra; and a second which was more heavily weighted in the lower troposphere, representing OCO retrievals.

Response matrices were then constructed for all 13 transport models as whole columns weighted according to the two vertical retrieval functions described above. All were regridded to the CSU 4x5 degree grid. Responses were built for vertically-weighted columns (representing the two satellite products), and for the flask sites, representing currently-available data.

Source/sink retrieval inversions were then performed on the synthetic data using each model's response function. Diagonal covariance matrices were used, with a uniform error representing unbiased satellite retrieval error, and cyclostationary (seasonal cycle) inversions were performed for each model's response function for each of 17 levels of retrieval error. Conceptually, the globally uniform error specified at each model grid cell represents retrieval error mitigated by averaging over a large number of retrievals in each model grid column in each month. On the other hand, real satellite retrievals will only sample certain locations in each grid column at certain times during each month, so the error budget should also include representation error in space and time. We assumed that the amount of representation error would scale with the monthly cloud fraction, since only clearsky retrievals are practical with OCO. Cloud fraction was specified from the1994 ISCCP product on a 2.5 degree equal area grid and monthly. A penalty function was calculated as $exp(1.5\, f_c^3)$, where f_c is the monthly mean fraction of the grid cell covered by clouds. This quantity was then used to inflate each given level of satellite retrieval error in order to increase the uncertainty where there is cloud cover.

In both cases, we added the satellite data to the current flask network, treated the uncertainty on the flask measurements as constant at the current value, and varied the error on the satellite observations between 0.1 ppm and 5 ppm (Fig 20). At 0.1 ppm, with perfect transport (achieved by using the same model to generate synthetic data and perform the inversion), the inversion returns nearly perfect estimates of the fluxes in every region. With a retrieval error of 5 ppm, the satellite adds very little information to the solution, which is only slightly better than the flask-only inversion.

As expected, adding transport error to the problem (by using one model to generate the observations and the others to perform the inversion) significantly reduces the advantage of the satellite observations. In the case of the thermal IR retrieval, the mean

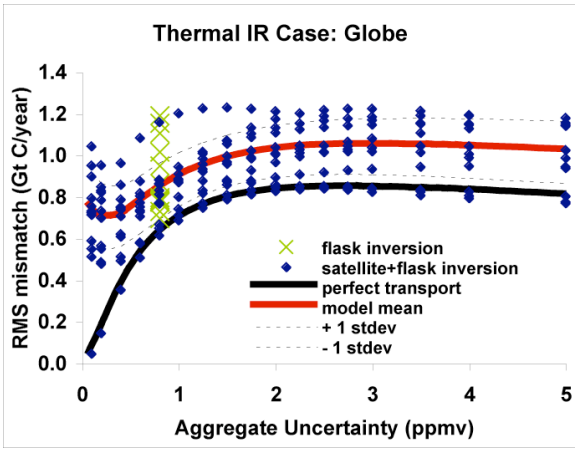

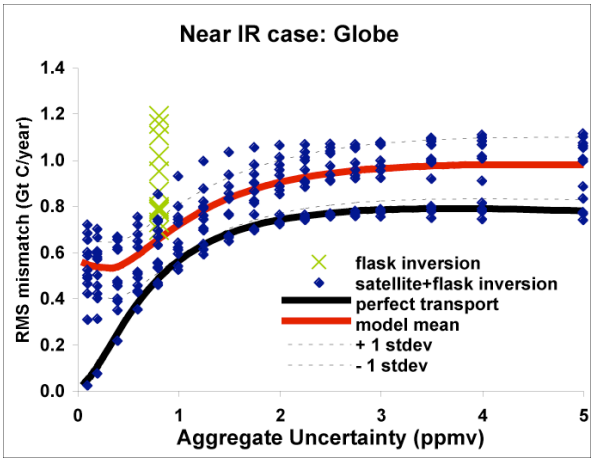

inversion with transport error does not improve over the flask-only inversion until retrieval error approaches 1 ppm. The result is somewhat better with the near-IR (OCO-like) inversions. Because the observations include near-surface fluctuations, they contain more information abut surface sources and sinks. Even with severe transport error, the satellite data improve the result relative to the flask-only inversions with retrieval errors as high as 2 ppm.

The ability of satellite observations to improve inversions in the face of transport error is not globally uniform (Fig 21). In Tropical America, for example, satellite data substantially improve flux estimates even in the presence of persistent clouds and significant transport error. This is because the flask constraint in that region is so weak. Over relatively well-observed North America, by contrast, the improvement over the flask-only inversions is less pronounced, even for the near-IR case.

2.6. Inversion method development

Global coverage by satellite observations requires new optimization techniques because Jacobian matrices involving hundreds of thousands of observations per day are simply too big to invert directly. We have experimented with two promising (and related) techniques for ensemble data assimilation.

In collaboration with Dr. Wouter Peters at NOAA CMDL, we have

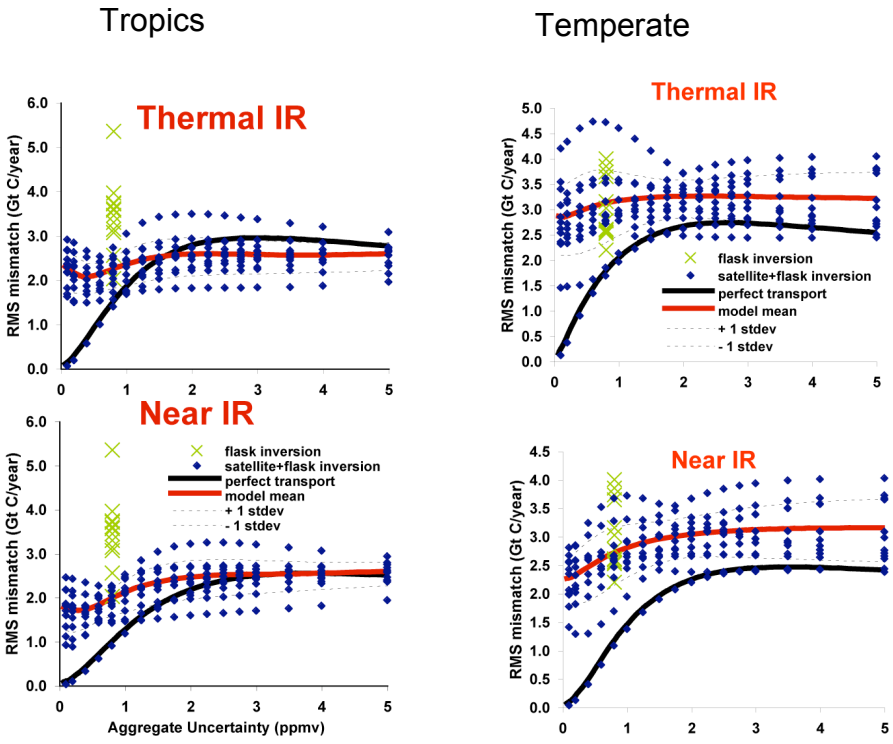

tested a system for atmospheric CO_2 data assimilation using the Ensemble Kalman Filter (EnKF). This method allows arbitrarily large observation vectors to be assimilated into a time- marched simulation of atmospheric transport and surface fluxes. Our work with NOAA on this project involved mostly a series of meetings and discussions of the ensemble assimilation method, which was implemented at NOAA. A publication explaining the system and demonstrating its capability is attached.

Work at CSU on ensemble data assimilation has continued, though we focus on a new optimization method called the Maximum-Likelihood Ensemble Filter (MLEF). Compared to EnKF, the MLEF is better suited to nonlinear problems, non-Gaussian errors in the observations, and the estimation of model error.

2.7. Synthetic datasets available

An important additional outcome of this research has been the production of a huge amount of synthetic (model-generated) atmospheric CO_2 data, which we have made available to other groups for their research on atmospheric retrieval and source inversions. We have worked closely with Randy Kawa at NASA GSFC to produce and evaluate global simulations of hourly surface CO_2 fluxes consistent with AVHRR NDVI and later SPOT and MODIS, and with the analyzed surface weathjer from the Goddard EOS Data Assimilation System. The hourly fluxes over land have been added to monthly mean fluxes due to fossil fuel combustion, air-sea gas exchange, and net sources and sinks estimated through the TransCom intercomparison. Finally, these fluxes were used to drive an atmospheric Parameterized Chemical Transport Model (PCTM) and produce global fields of simulated atmospheric CO_2 mixing ratio on a 1x1.25 degree grid on 25 levels. The evaluation of these data is ongoing, but preliminary results are very

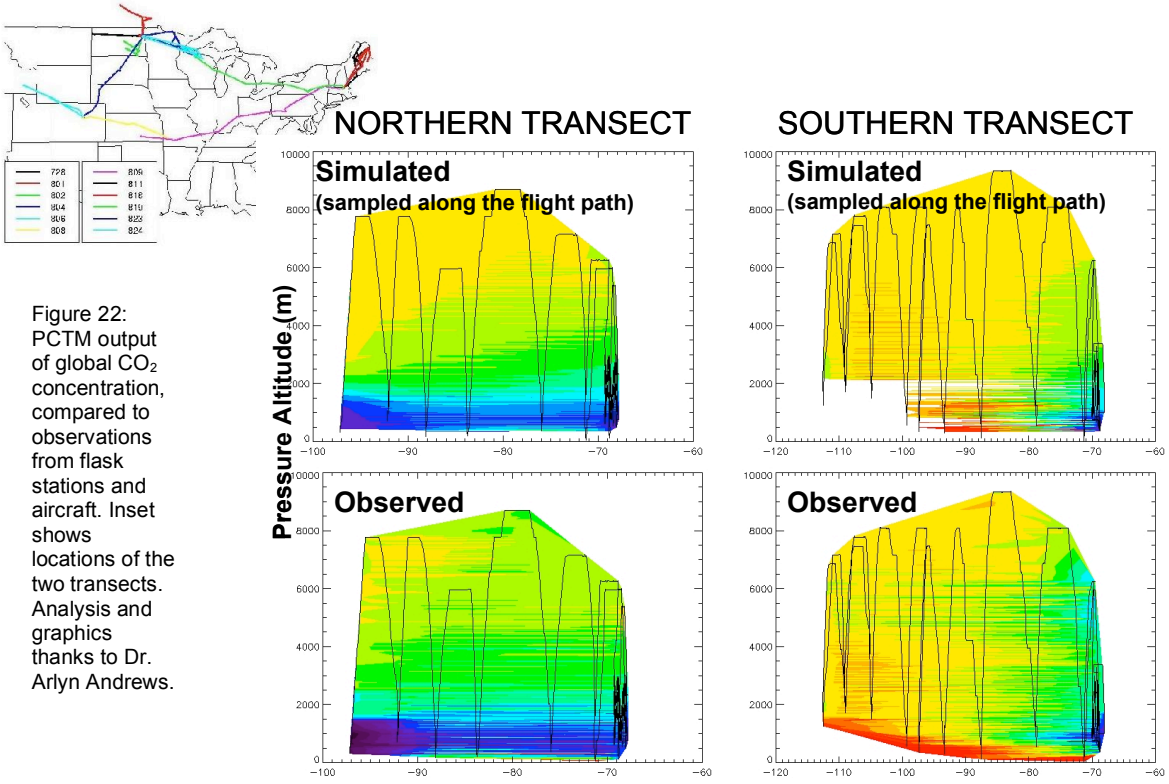

Figure 22: PCTM output of global CO_2 concentration, compared to observations from flask stations and aircraft. Inset shows locations of the two transects. Analysis and graphics thanks to Dr. Arlyn Andrews.

encouraging (Fig 22).

The global hourly fluxes used in these simulations have been provided to the global inverse modeling community for the years 2000-2003, and are expected to be the basis for a further model intercomparison activity of TransCom (simulations and evaluations of continuous records of CO_2 at in-situ observing locations, see http://transcom.colostate.edu).

In addition to the global synthetic data described above, we have developed nested mesoscale simulations over both North America and South America that include cloud-resolving grids over roughly 100x100 km areas for about two weeks each. These simulations represent self-consistent atmospheric conditions over an area roughly equivalent to a global model grid column, but which include heterogeneity resulting from realistic clouds, radiation, precipitation, and underlying variations in land cover and surface flux. They are the basis for our own research on clearsky sampling and representation error, as described above. We have also provided output from these high-resolution simulations to others in the OCO science team and at NASSA GSFC for their own experiments with synthetic data.

3. Graduate students supported

Kevin Gurney. Defended PhD, Towards robust regional estimates of carbon sources and sinks using atmospheric transport models., January, 2004. Started faculty position at Purdue University, September, 2005.

Mick Christy, Defended M.S., 2003, joined OCO Science Team. Accepted in PhD program, CSU, 2005.

Joanne Skidmore, Using Continuous [CO2] Data In Inverse Models To Reduce Uncertainty In Global And Regional Estimates Of Carbon Flux, M. S. April, 2004. Entered PhD program at SRON, The Netherlands.

Kathy Corbin, Evaluating Spatial, Temporal, and Clear-Sky Errors in Satellite CO2 Measurements, M. S., May 2005. Awarded NASA Earth System Science Fellowship and accepted into PhD program at CSU.

Aaron Wang, Observations And Simulations of Synoptic, Regional, and Local Variations of Atmospheric CO2 M. S. May 2005. Working as a Research Associate on aerosol-climate interactions at CSU.

4. Publications

4.1. Peer-reviewed Publications

Engelen, R.J., A.S. Denning, K.R. Gurney, 2002. On error estimation in atmospheric CO_2 inversions. Journal of Geophysical Research, 107, D22, doi:10.1029/2002JD002195.

Engelen, R.J., A.S. Denning, K.R. Gurney, G.L. Stephens, 2001. Global observations of the carbon budget. 1. Expected satellite capabilities for emission spectroscopy in the EOS and NPOESS eras. Journal of Geophysical Research, 106, D17, 20,055-20,068.

Christi, M. J., and G. L. Stephens (2004), Retrieving profiles of atmospheric CO_2 in clear

sky and in the presence of thin cloud using spectroscopy from the near and thermal infrared: A preliminary case study, J. Geophys. Res., 109, D04316, doi:10.1029/2003JD004058.

Peters, W., J.B. Miller , J. Whitaker , A.S. Denning , A. Hirsch , M.C. Krol , D. Zupanski, L. Bruhwiler, P.P. Tans. An ensemble data assimilation system to estimate CO_2 surface fluxes from atmospheric trace gas observations. J. Geophys. Res., in press.

Baker, D. F., R. M. Law, K. R. Gurney, P. Rayner , P. Peylin, A. S. Denning, P. Bousquet, L. Bruhwiler, Y.-H. Chen, P. Ciais , I. Y. Fung, M. Heimann, J. John, T. Maki, S. Maksyutov, K. Masarie, M. Prather, B. Pak, S. Taguchi, and Z. Zhu. TransCom3 inversion intercomparison: Impact of transport model errors on the interannual variability of regional CO_2 fluxes, 1988ñ2003. Global Biogeochem. Cycles, in press.

Bréon, F.-M., D. M. O'Brien, and J. D. Spinhirne, 2005: Scattering layer statistics from space borne GLAS observations. *Geophys. Res. Lett.* Submitted.

4.2. Additional Publications in Preparation

K.D. Corbin and A.S. Denning, Systematic differences in atmospheric CO_2 mixing ratio on clear vs cloudy days: Implications for satellite measurements. In preparation.

K.D. Corbin, A.S. Denning, A. Wang, I.T. Baker, and L. Lu. Using a high-resolution coupled ecosystem-atmosphere model to evaluate spatial, temporal, and clear-sky errors in satellite CO_2 retrievals. In preparation.

Aaron Wang, Observations And Simulations of Synoptic, Regional, and Local Variations of Atmospheric CO_2 M. S. May 2005.

Denning, A.S., K. R. Gurney, K. D. Corbin, M. J. Christy, Atmospheric inversion of satellie CO_2 mixing ratio in the presence of retrieval, sampling, and tracer transport error. In preparation.

4.3. Conference Presentations

Denning, A.S., 2001. Toward an Integrated Observing and Modeling Framework for Understanding and Predicting the Behavior of the Global Carbon Cycle (MC28). Presented at Sixth International Carbon Dioxide Conference, October 1-5, 2001, Sendai, Japan.

Denning, A.S., K.R. Gurney, R. Engelen, G. Stephens, D. OíBrien, P.J. Rayner and TransCom Modelers, 2001. Potential constraints on the global carbon budget using satellite retrievals of atmospheric CO_2. Presented at Sixth International Carbon Dioxide Conference, October 1-5, 2001, Sendai, Japan.

Denning A.S., M. Uliasz and J. Skidmore, 2002. Estimation of Regional Carbon Balance from Atmospheric Observations. A11E-03 Invited paper, American Geophysical Union Meeting, December 2002, San Francisco, CA.

Denning, A.S., M. Uliasz, K.J. Davis, and S. Richardson. (Invited) Regional Carbon Flux Estimation by Inversion of Mesoscale Tracer Transport, 2003 EOS Trans. AGU, 84(47), Fall Meet. Suppl., Abstract A51B-01 Invited.

Gurney, K.R., 2002. Taking Apart the Global Carbon Cycle: Where is the Missing Sink? Presented at University seminar, May 2002, University of California, Santa Barbara, CA.

Gurney, K.R., R. Law, A.S. Denning, P. Rayer, R. Dargaville, and TransCom 3 Modelers, 2002. Global-scale, seasonal carbon sources and sinks from the TransCom atmospheric inversion experiment. American Geophysical Union Meeting, December 2002, San Francisco, CA.

Schaefer, K., A. S. Denning, 2002. Estimating global carbon turnover times using data assimilation, Poster, American Geophysical Union Meeting, December 2002, San Francisco, CA.

Schaefer, K., A. S. Denning, N. Suits, J. Kaduk, I. Baker, S. Los, and L. Prihodko, 2003. The effect of climate on inter-annual variability of terrestrial CO_2 fluxes, Presentation, 83rd Annual AMS meeting, Feb. 2003, Long Beach, CA.

Skidmore, J., A.S. Denning, K.R. Gurney, K.J. Davis, and P.J. Rayner, 2003. Using Virtual Tall Tower CO_2 Data in Inverse Models to Reduce Uncertainty in Global and Regional Estimates of Carbon Flux. EOS Trans. AGU, 84(47), Fall Meet. Suppl., Abstract A52B-0786.

Uliasz, M. and A. S. Denning, 2002. Deriving Mesoscale Surface Fluxes of CO_2 from Concentration Data, Poster A12A-0141, American Geophysical Union Meeting, December 2002, San Francisco, CA.

Uliasz, M., 2002. Modeling framework to evaluate sampling strategies and estimate surface emissions of trace gases in mesoscale. 12th Joint Conference on the Application of Air Pollution Meteorology with the Air and Waste Management Association (A&WMA), May 20-23, 2002, Norfolk, VA.

Corbin, K., A.S. Denning, L. Prihodko, and M. Nicholls, 2003. Can Satellite Measurements Represent Regional Scale CO_2 Variability? EOS Trans. AGU, 84(47), Fall Meet. Suppl., Abstract A52B-0781.

Denning, A.S., M. Uliasz, K.J. Davis, and S. Richardson. (Invited) Regional Carbon Flux Estimation by Inversion of Mesoscale Tracer Transport, 2003 EOS Trans. AGU, 84(47), Fall Meet. Suppl., Abstract A51B-01 Invited.

Skidmore, J., A.S. Denning, K.R. Gurney, K.J. Davis, and P.J. Rayner, 2003. Using Virtual Tall Tower CO_2 Data in Inverse Models to Reduce Uncertainty in Global and Regional Estimates of Carbon Flux. EOS Trans. AGU, 84(47), Fall Meet. Suppl., Abstract A52B-0786.

Andrews, A.E., W. Peters, K. Schaefer, L. Bruhwiler, P. Bakwin, C. Zhao, J. Kofler, P. Tans, J. Lin, C. Gerbig, S. Wofsy, I. Baker, N. Suits, M. Uliasz, S. Denning, 2004: Coupling bottom-up and top-down approaches to understanding the carbon cycle: An analysis of data from the NOAA/CMDL WLEF-TV tall tower monitoring site in northern Wisconsin. EOS Trans, AGU, 85 (46) Fall Meet. Suppl., Abstract B22A-04.

Conner-Gausepohl, S., A. Denning, I. Baker, K. Gurney, J. Kleist, O. Leonard, J. Collatz, S. Kawa, S. Pawson, Z. Zhu, A. Andrews, 2004. Evaluation of simulated CO_2 using analyzed climate, transport and satellite vegetation. EOS Trans, AGU, 85 (46) Fall Meet. Suppl., Abstract B23A-0936.

Corbin, K., A.S. Denning, 2004: Will satellite CO_2 measurements experience a clear-sky bias? EOS Trans, AGU, 85 (46) Fall Meet. Suppl., Abstract A13A-0096.

Denning, S., M. Uliasz, D. Zupanski, J. Collatz, R. Kawa, K.R. Gurney, S. Conner-Gausepohl, A. Andrews, I. Baker, 2004: Diagnosis of the North American Carbon Cycle using data and models. EOS Trans, AGU, 85 (46) Fall Meet. Suppl. Abstract B22A-02.

O'Brien, D. M., and C. Anderson, 2005: Experiments with a neural network for OCO cloud detection. Presented at the OCO Science Team Meeting, California Institute of Technology, Los Angeles, 2005-03-22.

5. References

Baker, I.B., A.S. Denning, N. Hanan et al, 2003: Simulated and observed fluxes of sensible and latent heat and CO2 at the WLEF-TV tower using SiB2.5. *Global Change Biology*, **9**, 1262-1277.

Bakwin, P. S., P. P. Tans, D. F. Hurst, and C. Zhao, 1999. Measurements of carbon dioxide on very tall towers: results of the NOAA/CMDL program *Tellus*. 50B: 401-415.

Bakwin, P.S., K.J. Davis, C. Yi, S.C. Wofsy, J. W. Munger, L. Haszpra, and Z. Barcza, 2004: Regional

Carbon Dioxide Fluxes from Mixing Ratio Data. *Tellus*, **56B**, 301-311.

Baldocchi, D. D., 2003. Assessing the eddy covariance technique for evaluating carbon dioxide exchange rates of ecosystems: past, present and future. *Global Change Biology*, **9**, 479-492.

Bengtsson, L. and J. Shukla, 1988. Integration of space and in situ observations to study global climate change. *Bull. Amer. Meteor. Soc.,* 40, 1130-1143.

Bousquet, P., P. Peylin, P. Ciais, C. Le Quéré, P. Friedlingstein, and P. P. Tans, 2000. Regional changes in carbon dioxide fluxes of land and oceans since 1980. *Science*, 290: 1342-1346

Davis, K. J., D.H. Lenschow, S.P. Oncley, C. Kiemle, G. Ehret, A. Giez, and J. Mann, 1997: Role of Entrainment in Surface–Atmosphere Interactions over the Boreal Forest. J. Geophys. Res., 102, 29,219–29,230.

Davis, K. J., P.S. Bakwin, C. Yi, B.W. Berger, C. Zhao, R.M. Teclaw, and J.G. Isebrands, 2003: The Annual Cycle of CO2 and H2O Exchange Over a Northern Mixed Forest as Observed from a Very Tall Tower. Global Change Biology, 9, 1278–1293.

Denning, A.S., D.A. Randall, G.J. Collatz and P.J. Sellers, 1996: Simulations of terrestrial carbon metabolism and atmospheric CO2 in a general circulation model. *Tellus*, **48**B, 543-567.

Denning, A. S., M. Holzer, K. Gurney, M. Heimann, R. Law, P. Rayner, I. Fung, S. Fan, S. Taguchi, P. Friedlingstein, Y. Balkanski, J. Taylor, M. Maiss, and I. Lavin, 1999. Three-dimensional transport and concentration of SF_6: A model intercomparison study (TransCom2). *Tellus*, 51B, 266-297.

Enting, I. G., Trudinger, C. M., and Francey, R. J. 1995. A synthesis inversion of the concentration and $\delta^{13}C$ of atmospheric CO_2. *Tellus*, 47B, 35-52.

Enting, I. G., 2002. *Inverse Problems in Atmospheric Constituent Transport*, Cambridge Univ. Press, New York.

Fan, S., M. Gloor, J. Mahlman, S. Pacala, J. Sarmiento, T. Takahashi, and P. Tans, 1998. A large terrestrial carbon sink in North America implied by atmospheric and oceanic carbon dioxide data and models. *Science*, 282, 442-446.

Gloor, M., S.-M. Fan, S. Pacala, and J. Sarmiento, 2000. Optimal sampling of the atmosphere for purpose of inverse modelling: A model study. *Global Biogeochemical Cycles* 14: 407-428.

Gurney, K. R., R. M. Law, A. S. Denning, P. J. Rayner, D. Baker, P. Bousquest, L. Bruhwiler, Y-H Chen, P. Ciais, S. Fan, I. Y. Fung, M. Gloor, M. Heimann, K. Higuchi, J. John, E. Kowalczyk, T. Maki, S. Maksyutov, P. Peylin, M. Prather, B. C. Pak, B., J. Sarmiento, S. Taguchi, T. Takahashi, and C-W. Yuen, 2003. TransCom3 CO_2 inversion intercomparison: 1. Annual mean control results and sensitivity to transport and prior flux information. *Tellus*, 55B, 555-579.

Gurney, K. R., R. M. Law, A. S. Denning, P. J. Rayner, D. Baker, P. Bousquet, L. Bruhwiler, Y-H. Chen, P. Ciais, S. Fan, I. Y. Fung, M. Gloor, M. Heimann, K. Higuchi, J. John, T. Maki, S. Maksyutov, K. Masarie, P. Peylin, M. Prather, B. C. Pak, J. Randerson, J. Sarmiento, S. Taguchi, T. Takahashi, and C-W. Yuen, 2002. Towards robust regional estimates of CO_2 sources and sinks using atmospheric transport models. *Nature*, 415, 626-630.

Gurney, K. R., R. Law, P. Rayner, and A. S. Denning. Transcom 3 experimental protocol, *Atmos. Sci. Pap.* **707**, Department of Atmospheric Science, Colorado State University, 2000. (Available at http://transcom.colostate.edu/TransCom_3/T3_Protocol_and_Registration/body_t3_protocol_and_registration.html)

Gu, L., D. Baldocchi, S.B. Verma, T.A. Black, T. Vesala, E.M. Falge, and P.R. Dowty, 2002: Advantages of Diffuse Radiation for Terrestrial Ecosystem Productivity. J. Geophys. Res., 107 (D6), doi:10.1029/2001JD001242.

Hollinger, D.Y., F.M. Kelliher, J.N. Byers, J.E. Hunt, T.M. McSeveny, P.L. Weir, 1994: Carbon Dioxide Exchange between an Undisturbed Old-Growth Temperate Forest and the Atmosphere. Ecology, 75 (1), 134-150.

Houweling, S., F.M. Breon, I. Aben, C. Rödenbeck, M. Gloor, M. Heimann, and P. Ciais, 2004: Inverse Modeling of CO2 Sources and Sinks Using Satellite Data: A Synthetic Inter-Comparison of Measurement Techniques and their Performance as a Function of Space and Time. Atmos. Chem. Phys., 4, 523-538.

Los, S.O., G.J. Collatz, P.J. Sellers, et al, 2000: A Global 9-yr Biophysical Land Surface Dataset From NOAA AVHRR Data. *Journal of Hydrometeorology*, April 2000, 183-199.

Masarie, K. A. and Tans, P. P., 1996. Extension and integration of atmospheric carbon dioxide data into a globally consistent measurement record. *Jour. Geophys. Res.,* 100, 11593-11610.

Moeng, C.-H., 1984. A large-eddy simulation model for the study of planetary boundary layer turbulence. *Journal of Atmospheric Science*, 41, 2052-2062.

National Research Council (U.S.). Panel on Model Assimilated Data Sets for Atmospheric and Oceanic Research, 1991. *Four-Dimensional Model Assimilation of Data: A Strategy for the Earth System Sciences*. National Academy Press, Washington, D.C.

Pak, B.C. and Prather, M.J., 2001: CO2 Source Inversions Using Satellite Observations of the Upper Troposhere. Geophysical Research Letters, 28, 4571-4574.

Patra, P. K., and S. Maksyutov, 2002. Incremental approach to the optimal network

design for CO_2 surface source inversion. *Geophysical Research Letters*, **29**, NO. 10, 10.1029/2001GL013943.

Randerson, J. T., M. V. Thompson, T. J. Conway, I. Y. Fung, and C. B. Field, 1997. The contribution of terrestrial sources and sinks to trends in the seasonal cycle of atmospheric carbon dioxide. *Global Biogechemical Cycles*, **11**, 535-560.

Rayner, P. J., I. G. Enting, and C. M. Trudinger, 1996. Optimizing the CO_2 observing network for constraining sources and sinks. *Tellus*, **48B**, 433-444.

Rayner, P.J., and D.M O'Brien, 2001. The utility of remotely sensed CO_2 concentration data in surface source inversions, *Geophys. Res. Lett.,* 28, 175-178.

Sarmiento, J. L., S. C. Wofsy, E. Shea, A. S. Denning, W. Easterling, C. Field, I. Fung, R. Keeling, J. McCarthy, S. Pacala, W. M. Post, D. Schimel, E. Sundquist, P. Tans, R. Weiss, and J. Yoder, 1999. *A U.S. Carbon Cycle Science Plan*, Report of the Carbon and Climate Working Group, USGCRP, 69 pp.

Sellers P.J. and Mintz, Y., Y.C. Sud, A. Dalcher, 1986: A simple biosphere model (SiB) for use within general circulation models. *Journal of the Atmospheric Sciences*, **43**(6), 505-531.

Sellers, P.J. S.O. Los, C.J. Tucker, et al, 1996: A revised land surface parameterization (SiB2) for Atmospheric GCMs. Part I: Model formulation. *Journal of Climate*, **9**(4), 676-705.

Stephens, B. B., S.C. Wofsy, R.F. Keeling, and P. P. Tans, 1999. "The CO_2 Budget Rectification Airborne Study," AGU Geophysical Monograph on *Inverse Methods in Global Geochemical Cycles*.

Stull, R. B., 1994. *An Introduction to Boundary Layer Meteorology*. Kluwer Academic Publishers, 666 pp.

Suntharalingam, P. D.J. Jacob, P.I. Palmer, J.A. Logan, R.M. Yantosca, Y. Xiao, M.J. Evans, D.G. Streets, S.L. Vay, and G.W. Sachse, 2004: Improved Quantification of Chinese Carbon Fluxes using CO2/CO Correlations in Asian Outflow. J. Geophys. Res., 109, doi:10.1029/2003JD00436

Tans, P.P., P.S. Bakwin, and D.W. Guenther, 1996. A feasible Global Carbon Cycle Observing System: A plan to decipher today's carbon cycle based on observations. *Global Change Biology* **2**, 309-318.

6. Papers attached as PDF files

Engelen, R.J., A.S. Denning, K.R. Gurney, 2002. On error estimation in atmospheric CO_2 inversions. Journal of Geophysical Research, 107, D22, doi:10.1029/2002JD002195.

Engelen, R.J., A.S. Denning, K.R. Gurney, G.L. Stephens, 2001. Global observations of the carbon budget. 1. Expected satellite capabilities for emission spectroscopy in the EOS and NPOESS eras. Journal of Geophysical Research, 106, D17, 20,055-20,068.

Christi, M. J., and G. L. Stephens (2004), Retrieving profiles of atmospheric CO_2 in clear sky and in the presence of thin cloud using spectroscopy from the near and thermal infrared: A preliminary case study, J. Geophys. Res., 109, D04316, doi:10.1029/2003JD004058.

Peters, W., J.B. Miller , J. Whitaker , A.S. Denning , A. Hirsch , M.C. Krol , D. Zupanski, L. Bruhwiler, P.P. Tans. An ensemble data assimilation system to estimate CO_2 surface fluxes from atmospheric trace gas observations. J. Geophys. Res., in press.

Baker, D. F., R. M. Law, K. R. Gurney, P. Rayner , P. Peylin, A. S. Denning, P. Bousquet, L. Bruhwiler, Y.-H. Chen, P. Ciais , I. Y. Fung, M. Heimann, J. John, T. Maki, S. Maksyutov, K. Masarie, M. Prather, B. Pak, S. Taguchi, and Z. Zhu. TransCom3 inversion intercomparison: Impact of transport model errors on the interannual variability of regional CO_2 fluxes, 1988ñ2003. Global Biogeochem. Cycles, in press.